Probing Ising Superconductivity and Light-Induced Phase Transitions in Two-Dimensional
Transition Metal Dichalcogenides

by

Tina Elayne Dekker

A thesis
presented to the University of Waterloo
in fulfillment of the
thesis requirement for the degree of
Master of Applied Science
in
Electrical Engineering – Nanotechnology

Waterloo, Ontario, Canada, 2019

AUTHOR'S DECLARATION

This thesis consists of material all of which I authored or co-authored: see Statement of Contributions included in the thesis. This is a true copy of the thesis, including any required final revisions, as accepted by my examiners.

I understand that my thesis may be made electronically available to the public.

Statement of Contributions

Chapter 4 contains content from a manuscript in preparation for publication. The manuscript is written by Prof. German Sciaini and Dr. Nicolas Rivas, and co-authored by myself, my supervisor (Prof. Adam Wei Tsen), Dr. Ariel Petruk, Shazhou Zhong, and Dr. Kostyantyn Pichugin. For this project, I primarily fabricated samples for measurements on chips prepared by Dr. Petruk. Dr. Rivas performed the pump-probe spectroscopy measurements and corresponding data analysis. Transport measurements were jointly completed by myself and Shazhou Zhong. The two-band model fit applied to the transport measurements was calculated by Shazhou Zhong.

Abstract

2H-NbSe$_2$ is a superconducting transition metal dichalcogenide that retains its superconductivity in its two-dimensional (2D) form. Owing to strong spin orbit coupling, 2D 2H-NbSe$_2$ demonstrates unconventional superconductivity that allows both spin-singlet and spin-triplet Cooper pairing. There is experimental and theoretical evidence that 2D 2H-NbSe$_2$ is an Ising superconductor. However, a direct measurement of its Ising nature has not yet been proven. In this thesis, I present the results of measurements on a 2H-NbSe$_2$ superconducting spin filter tunnel junction fabricated with mechanically exfoliated 2D flakes. Using this device geometry, it may be possible to elucidate the pairing nature in 2H-NbSe$_2$.

Intense ultrashort laser pulses can photo-excite non-equilibrium states in materials leading to transient new phases and exotic states. In bulk materials these photo-excited states are short-lived. 1T′-MoTe$_2$ in bulk form undergoes a reversible transition at ~250 K from the monoclinic phase (1T′-MoTe$_2$) to the inversion-symmetry breaking, orthorhombic phase (T$_d$-MoTe$_2$). T$_d$-MoTe$_2$ is a candidate type II Weyl semimetal that is predicted to demonstrate exotic quantum phenomena. These phases in 2D MoTe$_2$ flakes are characterized using ultrafast optical-pump probe techniques. The results indicate a permanent photo-induced structural change occurs in thin T$_d$-MoTe$_2$ at high fluences. Given the durability of this structural change, further characterization of the sample is achieved using magnetotransport measurements.

Acknowledgements

I would first like express my gratitude to Adam Wei Tsen, my primary supervisor, for his guidance through many research projects over my degree and his advice during various stages of my writing process. I am also very appreciative of the advice by my other supervisor, Na Young Kim, who always found positivity and opportunity within the various challenges that arose in my research.

I am thankful for the valuable support from all of the members of the Tsen Group. For the projects in this thesis, special thanks go out to Hyun Ho Kim for his help in developing effective fabrication techniques with me, as well as to Joey (Shazhou) Zhong and Archana Tiwari for assisting me with transport measurements when needed. Joey also aided me in the editing of some sections of my thesis.

Peter Sprenger managed the ^{3}He cryostat for the transport measurements. I am appreciative of the time and effort he puts in to ensure that our group's measurements are always in optimal conditions.

Table of Contents

List of Figures

List of Tables

Chapter 1

Introduction

1.1 Two-Dimensional (2D) Materials

In 2004, K. S. Novoselov and A. K. Geim successfully isolated monolayer graphene using a mechanical exfoliation technique with ordinary adhesive tape that later earned them the 2010 Nobel Prize in Physics [1], [2]. This new technique of isolating mono- and few-layer flakes from layered materials transformed the field of 2-dimensional (2D) material research. Previously, thin films were almost exclusively fabricated from a bottom-up approach, using growth methods such as chemical vapour deposition (CVD) and molecular beam epitaxy (MBE) [3]. These methods are expensive, time consuming, and growing high quality monolayer films is difficult. The types of materials and epitaxially grown heterostructures are also limited. With Novoselov and Geim's new technique of isolating layered materials, many high quality 2D materials became experimentally accessible with the advantage of being able to form unique heterostructures. Transition metal dichalcogenides (TMDs) have particularly garnered immense interest due to unique phenomena that are predicted to occur in their isolated 2D forms that can be harnessed for optoelectronics [4], [5], sensors [6], spintronics [7]–[9] and other electronic devices [10]. Some TMDs in their 2D form are also candidates to realize non-trivial topological phases [11]–[13].

An example of a 2D TMD expected to have unique application is $2H$-$NbSe_2$, for which the first 2D measurement of superconductivity was realized [14]. This material is known to exhibit the coexistence of charge density waves and superconductivity at low temperatures and, compared to other 2D materials, does not require gating or pressure to achieve these states [15], [16]. It is also one of few materials to feature unconventional Ising superconductivity [17]. Another material of great interest is T_d-$MoTe_2$, which is predicted to host type-II Weyl fermions and thus demonstrate unique quantum transport phenomena. Overall, these materials offer opportunity to understand fundamental and new quantum phenomena that may be eventually engineered to realize novel quantum devices.

1.2 Transition Metal Dichalcogenides

TMDs are layered van der Waals (VDW) materials with a structure of MX_2, where M is a transition metal (e.g. Mo, W, etc.) and X is a chalcogen atom (S, Se, etc.). A monolayer TMD consists of an atomic layer of transition metal atoms that are covalently bound and sandwiched between two

chalcogen atomic layers. The weak VDW forces between chalcogen layers and strong in-plane covalent bonds allow TMD layers to be easily separated into pristine mono- and few-layer flakes via exfoliation techniques. TMDs typically crystallize into either the 2H or 1T phases, where the 2H phase is usually semiconducting and the 1T phase is usually metallic. Some materials can also acquire the metastable 1T′ phase, which features an in-plane distortion. Many of the first studies of TMDs used the semiconducting TMDs due to their stability in air [18]. However, more exotic and metallic TMDs (e.g. 1T′-$MoTe_2$, 1T-TaS_2, etc.) require handling in an inert environment and must have a protective capping layer for transit in ambient air.
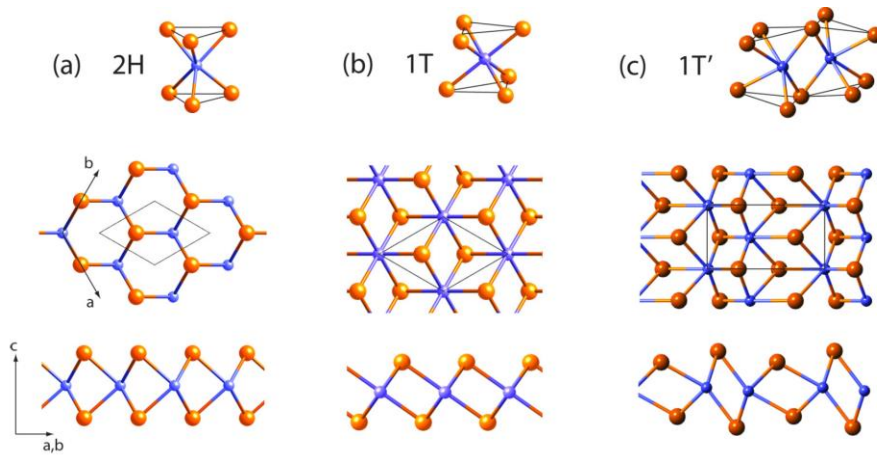
Figure 1: a) 2H, b) 1T, and c) 1T′ phases of $MoTe_2$ [19].

Important to the study of 2D TMDs is the change in band structure as the materials are reduced to few-layer flakes. The first Brillouin zone and MoS_2 band structure as function of thickness are shown in Figure 2. Many semiconducting TMDs, for example, will transition from indirect to direct band gap semiconductors at the monolayer limit. The first Brillouin zone of all TMDs is hexagonal and features degenerate, inequivalent valley pairs at the ±K symmetry points. Most changes to the band structure at the 2D limit occur at these symmetry points [20], [21]. Strong spin orbit coupling (SOC) attributed to the large atomic mass of transition metals results in spin orbit splitting of the valence and conduction bands [9], [22]. For the valence and conduction bands respectively, this splitting energy is on the order of 100's of meV and several meV. Monolayer TMDs also demonstrate broken inversion symmetry that, together with strong SOC, causes strong coupling between the spin and valley degrees of freedom. This spin-valley locking necessitates opposite spins in the spin-split valleys and sustains the polarization in the absence of a magnetic field. The band structure of 2D TMDs is what creates many opportunities to realize unique electronic properties in these materials [23].

2

(a)

(b)

| Bulk | 4-layer | Bilayer | Monolayer |

Energy

Γ M K   Γ Γ M K   Γ Γ M K   Γ Γ M K   Γ
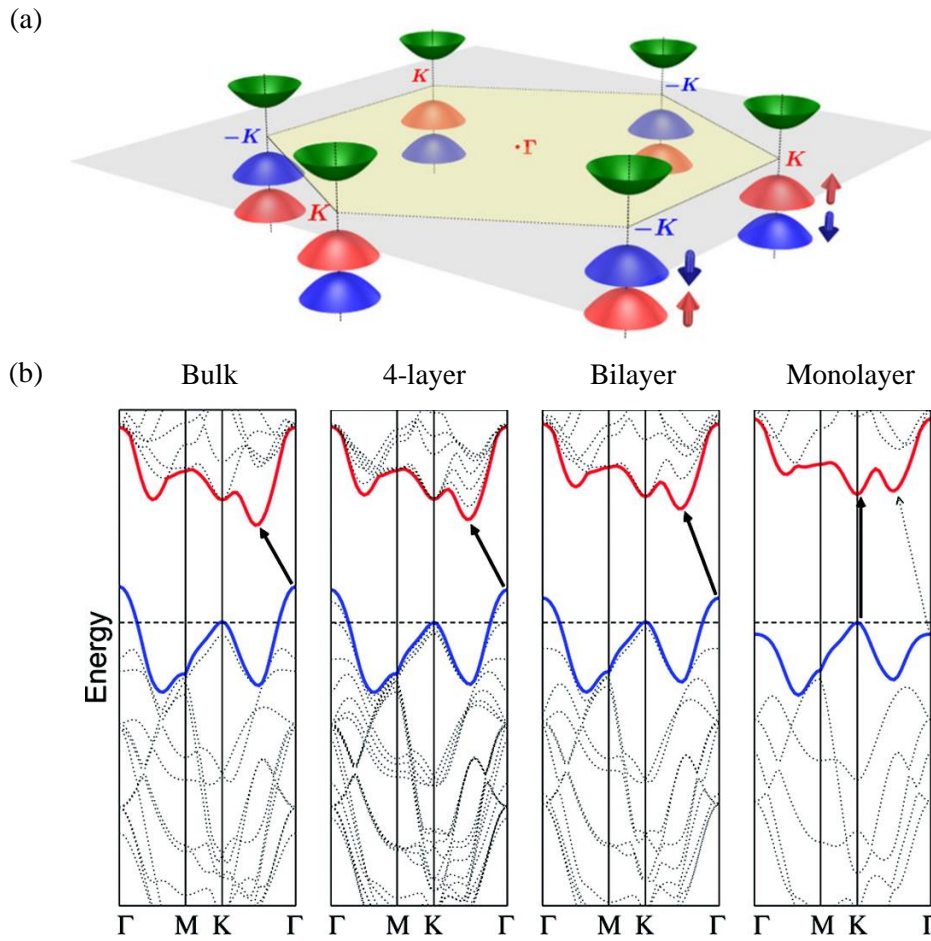
Figure 2: a) First Brillouin Zone of a monolayer TMD showing spin orbit split bands and spin-locked index [22]; b) MoS₂ band structure as a function of thickness [20].

1.3 Heterostructures

A notable advantage of fabricating devices with exfoliated VDW materials is the nearly unrestricted opportunity to interface these materials in unique geometries that would be difficult or impossible with growth methods. There are, however, limitations. First, it should be noted that mechanical exfoliation and its accompanying device fabrication techniques are not suitable for mass production. Large scale integration of technologies involving 2D VDW materials still require standard growth and fabrication techniques, which immediately imposes limitations due to film quality, thermal budget, etc.. As such, mechanical exfoliation and transfer techniques are better suited for fundamental research where interfaces and device geometries can be precisely configured to observe unique physical properties and phenomena.

Another limitation exists from the fact that materials such as graphene and MoS_2 are archetypal VDW materials. They have low cleavage energies that allow for easy exfoliation and they are stable in ambient air [24]. The reality is that many of the interesting VDW materials are metastable in their isolated 2D form and easily oxidize, or even degrade. This was demonstrated by Tsen *et al.*, who show the formation of oxide layers on thin, metallic $1T\text{-}TaS_2$ using scanning transmission electron microscopy (STEM), shown in Figure 3 [25]. They found that oxidation of the sample inhibited charge ordering. Obviously, the presence of an oxide on a 2D material can significantly affect material properties and interfere with interfacial phenomena. Therefore, fabrication in an inert environment is required.
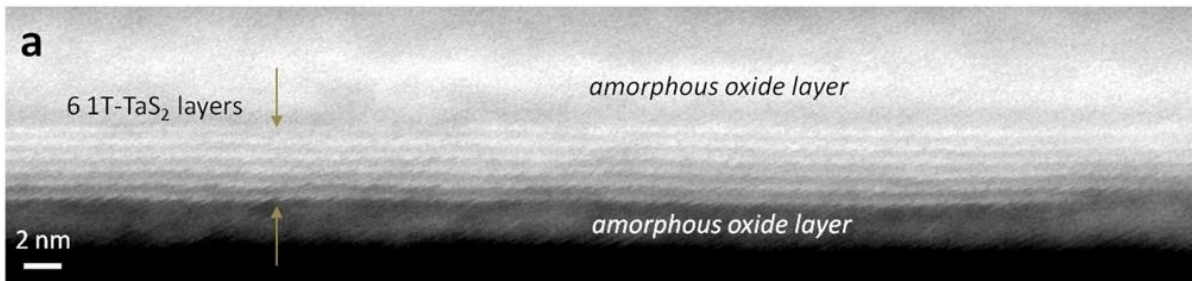
Figure 3: STEM image of 6-layer $1T\text{-}TaS_2$ exposed to air [25].

Inspired by the exfoliation of graphite (Gr), exfoliation of hexagonal boron nitride (hBN) soon followed [26], [27]. This insulating material has a hexagonal, layered structure similar to graphite, but substitutes carbon atoms for boron and nitrogen atoms. Due to its semi-transparency, insulating behaviour, and easy exfoliation, 2D hBN is extraordinarily useful for the fabrication of

heterostructures. In its most basic use, hBN is used to cap sensitive 2D materials as protection from oxidation. However, it is also used to provide an atomically flat surface on which to transfer other exfoliated flakes, as an atomically thin oxide layer in tunneling devices or transistors, among other creative applications [28], [29].

Integral to the exfoliation of VDW materials is the subsequent transfer methods required to form devices from exfoliated flakes. Most transfer methods use a polymer stamp as the medium by which exfoliated flakes are transferred to the final substrate. Overall, the ability to fabricate unique heterostructures using exfoliated VDW materials offers many opportunities to tune material and device properties. In optoelectronics, a common application is to combine two TMDs with type II band alignment to observe and harness interlayer excitons [5], [30], [31]. Similarly, atomically thin VDW materials are a predicted route to topological phases [9], [11], [13], [25].

1.4 Thesis Outline

This thesis is structured into three topics. First, general fabrication methods are described in Chapter 2. Different VDW materials require different exfoliation techniques based on their stability and strength of interlayer forces. Forming complex heterostructures requires careful techniques for picking up the flakes and transferring them to the desired substrate. Maintaining clean interfaces and achieving good contact with electrodes are pervasive problems in the field of 2D materials. These challenges are discussed.

Chapter 3 presents the theory and results of a spin polarized tunneling measurement of superconducting 2D 2H-NbSe$_2$ (written henceforth as NbSe$_2$). NbSe$_2$ is one of few materials that retains its superconductivity when isolated to its 2D form [32]. Both theoretical [33] and experimental [17], [34], [35] studies have revealed that 2D NbSe$_2$ demonstrates Ising superconductivity. However, a spin polarized tunneling measurement of NbSe$_2$ that elucidates the spin-triplet and spin-singlet pairing nature has not yet been done. A spin polarized measurement of NbSe$_2$ requires half-metal leads or a spin filter tunnel junction. The challenge for these geometries is finding a suitable 2D ferromagnet with strong polarization. The discovery of 2D magnetic materials with high polarizability and compatibility with existing exfoliation and heterostructure fabrication techniques overcomes this challenge [36], [37]. A spin polarized tunneling measurement of superconductivity in NbSe$_2$ can theoretically be realized using a junction of NbSe$_2$, the ferromagnetic semiconductor CrBr$_3$, and graphite as a metallic lead.

Chapter 4 describes a study of the orthorhombic and monoclinic phases of $MoTe_2$. The low temperature orthorhombic (T_d) phase of $MoTe_2$ is predicted to host type II Weyl fermions [12], [13]. Type II Weyl semimetals have contact points between the electron and hole pockets, called Weyl nodes. These protected crossings are robust against small perturbations and manifest in unique physical phenomena. Weyl nodes can only appear in materials that either break time-reversal symmetry or have broken inversion symmetry [38]. The orthorhombic phase of $MoTe_2$ has broken inversion symmetry, thus satisfying this primary requirement to realize Weyl nodes. $1T'$-$MoTe_2$ undergoes a reversible phase transition to T_d-$MoTe_2$ at temperatures below ~250 K [39]. A greater understanding of these two $MoTe_2$ phases and the dynamics of the transition between them is thus desirable. In a collaboration with Prof. Sciaini's research group at the University of Waterloo, we study these two phases using femtosecond broadband pump-probe spectroscopy. Using ultrafast pump-probe techniques, we are able to observe the characteristic vibrational Raman modes of the $1T'$- and T_d-phases of $MoTe_2$ and follow their temporal evolution. This chapter details the results of these measurements and discusses structural changes observed by irradiating T_d-$MoTe_2$ with high fluences.

Chapter 2

General Experimental Methods

2.1 Exfoliation and Transfers of 2D Materials

Since the first isolation of graphene using 3M Scotch tape [1], optimized exfoliation methods and techniques for transferring exfoliated flakes have been widely studied [40]–[46]. Exfoliation methods primarily rely on using an adhesive tape to thin bulk VDW materials. The choice of tape (and its adhesion properties) is generally a preferential choice of the user. 3M Scotch tape is suitable for most applications. A small piece of bulk crystal is placed on the tape which is then folded over 2-5 times without overlapping the exfoliated crystal pieces. The tape is then transferred to another medium which further exfoliates the material, ideally leaving few-layer or monolayer flakes on the medium. From this point, the flakes can be transferred or picked up to form heterostructures, transferred to prepatterned electrodes, or subjected to other processes (electrode post-patterning, annealing, etc.).

Unfortunately, many creative transfer techniques or post processing methods are only possible with archetypal materials like graphite and MoS_2, which are not very sensitive the ambient environment and have stable crystal structures. Many of the exotic VDW materials are metastable and thus extremely sensitive to oxidation, and often other variables such as temperature and strain. As a result, the polymer stamp transfer method remains the most feasible. This chapter reviews the two primary polymer stamp methods that are used and provides a brief discussion on substrates and measuring flake thicknesses. The traditional polydimethylsiloxane (PDMS) stamp method is used to fabricate samples for the $MoTe_2$ broadband impulsive vibrational spectroscopy measurements. The more advanced and versatile "PC" method is used to fabricate the $NbSe_2$ superconducting spin filter tunnel junction.

2.1.1 Substrates

The choice of substrate is undeniably an important factor for any device. The dominance of silicon-based substrates in the semiconductor industry makes Si/SiO_2 the natural choice for most electronic and optoelectronic applications. This is, in part, due to the well-established fabrication methods developed for silicon technology. In an ideal 2D electronic device that uses exfoliated VDW materials, the flakes are first transferred to a Si/SiO_2 substrate and then electrodes are post-patterned onto the flake(s) to make electrical contact. This offers significant flexibility in device design; the

flake dimensions are easier to accommodate, complex devices using multiple embedded electrodes are possible, and the conformal nature of deposition techniques promotes less resistive electrical contact with the flakes. However, the major drawback of post-patterned electrodes is that the device must be exposed to ambient air in transit to different instruments. Also, the solvents and heating required by standard photolithography techniques can damage or oxidize sensitive materials. For this reason, pre-patterned electrodes are often preferable. The main advantage of pre-patterned electrodes is that devices can be fabricated and encapsulated in an inert environment, after which they can be safely transported in ambient air. The drawbacks for pre-patterned electrodes are that the flake dimensions have more stringent requirements, there is generally less flexibility in heterostructure design, and the electrical contact between the electrode and flake can be quite resistive.

In general, while post-patterned electrodes can sometimes offer better electrical contact, the reality is that achieving ohmic contact in any geometry with 2D semiconducting materials is a pervasive problem in the field [47]–[49]. Many methods have been developed to improve electrical contact with exfoliated 2D materials, including a one-dimensional edge contact [46], phase engineering [50], and doping [10]. When applicable, it is easier to use graphite or graphene as an intermediate layer between a flake and a pre-patterned electrode. This is the method employed for the $NbSe_2$ device in this thesis.

For optical measurements in a transmission geometry, such as that used in this thesis, Si/SiO_2 is not suitable for the devices because it is not transparent. Even though thin films of Si and SiO_2 can be transparent to the wavelengths of the incident light, the thickness of the substrate itself completely attenuates any transmitted signal. In this case, silicon nitride (Si_3N_4) windows can be fabricated on Si/SiO_2 that offers transparency for transmissive optical experiments. This process is described in more detail in Section 4.2.1.

2.1.2 Polydimethylsiloxane (PDMS) Transfer Method

The PDMS method may be considered as the traditional method of exfoliation. Thin PDMS stamps (~5 mm thick) are cut into ~1 cm x 1 cm pieces and placed on a clean glass slide. 3M Scotch tape with mechanically exfoliated crystals is carefully placed on the PDMS. A cotton swab or other rounded surface is used with very light pressure to improve the contact between the flakes and the PDMS. The tape is then removed quickly in a single motion (like ripping a bandage), leaving behind further exfoliated flakes. The glass slide is attached to a transfer stage, consisting of a micromanipulator coupled to an optical digital microscope (Olympus), and analyzed for flakes. A

schematic of a transfer stage is shown in Figure 4a. A basic transfer stage requires x-, y-, and z-axis manipulation. The transfer stage used for the devices of this thesis is shown in Figure 4b. The stage has a ceramic heater on a rotational stage that can rotate 360° (Θ). Both the microscope and the manipulator have 3 spatial degrees of freedom (x, y, z), and the manipulator, which holds the glass slide, can additionally be tilted up to 360° (φ).

(a)
(b)
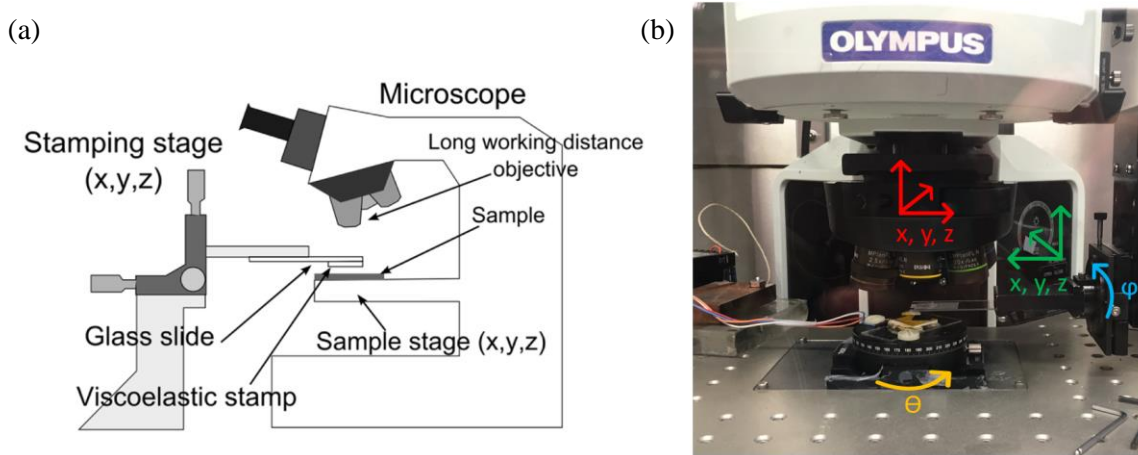
Figure 4: a) Transfer stage schematic [40]; b) Actual transfer stage in nitrogen glovebox.

The manipulator is used to scan the PDMS for flakes. The thickness of flakes can be approximated based on optical contrast, according to previously measured flakes (e.g. using atomic force microscopy) and prior experience. Determining flake thickness, notably for seeing monolayers like graphene [51], is most effective on silicon with a silicon dioxide layer ~300 nm thick (Si/SiO_2). When a suitable flake is found, it can be transferred to a substrate using the transfer stage. In this thesis, p-type silicon (B) with a 285 nm silicon dioxide thickness is always used and is simply referred to as silicon. The silicon is fixed to the stage with double-sided Kapton tape and the flake is positioned roughly above the location where it will be transferred. The objective is focused on the substrate, then focused slightly above the substrate. The glass slide is carefully lowered (z-axis) until the flake reaches the focal plane. This process is repeated, with lateral adjustments of the x- and y-axes, until the PDMS just makes contact. The contact boundary is easily distinguished: it is a greenish colour compared to the purplish colour of the silicon substrate. The PDMS is slowly brought into contact with the substrate until the flake is also in contact. The viscoelastic nature of PDMS is the driving nature of these transfers. When PDMS is lifted very slowly from the substrate, the polymeric chains constituent to the PDMS have time to reorganize to an energetically favourable state, which in this context means releasing the flake from the PDMS onto the substrate. Heating the substrate after

9

making contact promotes polymeric chain motion and facilitates the transfer process. Usually temperatures between 60 °C to 100 °C suffice, but room temperature transfers are also feasible, especially for thicker flakes (>20 nm).

The PDMS transfer technique is popular due to its ease and efficacy. A major drawback of the PDMS method is that PDMS leaves residue on flakes, even for room temperature transfers. Moderate annealing and/or chemical cleaning cannot completely remove this residue and these processes are often not suitable for sensitive materials anyway. Fabricating complex heterostructures is also very difficult with PDMS. First, the interfaces between flakes will not be pristine due to residue. PDMS transfers can also crack flakes, shift the flake positions during transfers, and occasionally pick up already transferred flakes. For simple devices made of only a few flakes, and where interfacial phenomena are irrelevant, the PDMS transfer method is appropriate. For complex structures, or studies where interfacial phenomena are relevant, the so-called "PC" method is better.

2.1.3 "PC" Transfer Method

The "PC" method is the current method used for fabricating high quality TMD heterostructures. This method uses a type of polycarbonate (hence, "PC"), which is synthesized into a thin film and placed on a small piece of PDMS. Using similar transfer techniques as for the PDMS method, the PC is manipulated above and below its glass transition temperature to pick up flakes in succession from silicon substrates. The VDW materials are exfoliated directly onto silicon chips using tape. An hBN flake is picked up first as a support layer and then used to pick up subsequent flakes; it also serves as a protective capping layer. Once the desired flakes have been picked up, the entire stack is transferred to the final substrate by melting the PC and then removing it afterwards with solvent.

The advantage of this method is that complex heterostructures can be formed with pristine interfaces, albeit bubble formation does occur across flake overlap areas greater than several micrometers squared. These bubbles contain either air or adsorbents (hydrocarbons, water, etc.) and will occur regardless of transfer technique. The transfer success rate of the PC method is much higher than the PDMS method. There are no major disadvantages to the PC method, besides that it less straightforward than the PDMS method and requires more time. While high temperatures (greater than 150 °C) are required, materials that are typically sensitive to heat (e.g. $1T\text{-}TaS_2$, $1T'\text{-}MoTe_2$) seem to be unaffected, likely due to the protective hBN layer used to pick up the flakes.

2.2 Atomic Force Microscopy

The thickness of 2D materials is very important to the electronic and optical properties of the material. During the fabrication process, it is useful to use the optical contrast of exfoliated flakes to estimate thickness. This is especially important for materials that must be fabricated in an inert environment. It is possible to measure the true thickness of flakes in a heterostructure using atomic force microscopy (AFM). AFM is a form of scanning probe microscopy that, in its most basic use, maps the topology of a surface with nanometer resolution. Sub-nanometer resolution is possible in the z-axis (normal to the substrate) for instruments well protected from noise. This characterization method is non-destructive and relatively simple to use. Owing to the conformal contact of 2D flakes, the AFM tip can resolve the difference in thickness between a flake that encapsulates another flake. Usually hBN or graphene are used as capping materials, however, the principle applies for any overlapping 2D flakes. This does introduce a small error in the measurement of the encapsulated flake since there is still some finite space between the flakes. This error is negligible but is cumulative as more flakes are stacked on top of each other. One can also assume a greater error for thicker encapsulating flakes. Generally, the encapsulating flake should be ~20 nm thick or less for best results. As an example, Figure 5 shows a schematic depicting this method on an hBN encapsulated MoTe$_2$ sample with its AFM trace.
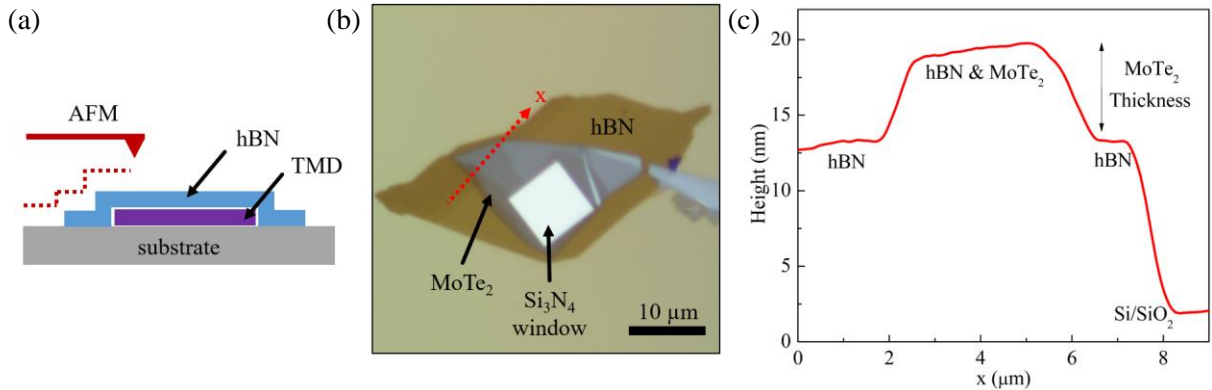
Figure 5: a) Schematic showing the principle of AFM on encapsulated TMD flakes; b) Representative MoTe₂ sample encapsulated with hBN with c) corresponding AFM trace.

Chapter 3

Superconducting Spin Filter Tunnel Junction

3.1 Overview: Probing the Pairing Nature in 2D 2H-NbSe$_2$

This chapter presents the theory of the superconducting nature of 2D NbSe$_2$ and the results of measuring a superconducting spin filter junction. The superconductivity of NbSe$_2$ is governed by Ising spin orbit coupling (SOC), which allows both spin-singlet and spin-triplet Cooper pairing in the superconducting state. By performing a spin polarized tunneling measurement on 2D NbSe$_2$, further insight on this pairing is possible [17], [33].

It is predicted that the application of an in-plane magnetic field to a device consisting of an Ising superconductor and a half-metal lead will enhance the measured conductance [33]. This occurs because spin-singlet pair tunneling is restricted, thus allowing only spin-triplet pairs, which are oriented to the in-plane direction, to tunnel through the junction. CrBr$_3$ is a layered material with ferromagnetic ordering between layers and strong polarization in its 2D form, suggesting it can be used as an efficient spin filter. Measurements on a Gr-CrBr$_3$-NbSe$_2$ superconducting spin filter junction (SFTJ) are discussed. The thickness of the CrBr$_3$ junction ultimately imposes an insurmountable trade-off between spin filter performance and tunneling efficiency [52].

3.2 Ising Superconductivity in NbSe$_2$

3.2.1 Superconductivity

Superconductivity is the phenomenon where the resistance of a material becomes zero below some critical temperature (T_c) and the material demonstrates the Meissner effect by expelling magnetic fields from the bulk material. The breakdown mechanisms due to an external magnetic field of type I and type II superconductors can be categorized by spin alignment and orbital effects, respectively. Type I superconductors have a single temperature dependent critical field, H_c, where a first order phase transition to the normal state occurs when Cooper pairs are broken by spin alignment with the magnetic field. Type II superconductors are characterized by a continuous breakdown of superconductivity due to orbital effects which form magnetic vortex cores in the material. This results in the lower and upper critical fields, H_{c1} and H_{c2}. Above the lower critical field (H_{c1}) vortex formation creates a mixed normal and superconducting state in the material. As the magnetic field

increases, the vortex density increases until adjacent vortices are in contact at a critical field strength (H_{c2}), where the superconductor transitions to the normal state [53].

A conventional superconductor can be described completely by the Bardeen-Cooper-Schrieffer (BCS) theory of superconductivity or by any of its extensions. BCS theory is a microscopic description of superconductivity, where electrons of opposite spin in the superconductor interact with phonons to form bound pairs in a singlet state and are called Cooper pairs [54]. At low temperatures (below T_c), there is a condensation of these boson-like pairs. In order to break apart a Cooper pair, the energy required is the energy necessary to break all of the Cooper pairs in the condensate. The result is a temperature dependent energy gap (Δ) between the ground state and quasi-particle excitations, given by:

$$\Delta(T = 0) = 1.764 k_B T_c, \tag{1}$$

where k_B is the Boltzmann constant. With a sufficiently large external magnetic field, Cooper pairs in type II superconductors are broken due to coupling between the field and the electron orbital and spin degrees of freedom [34]. At this point, the superconducting gap vanishes and the material is in the normal state.

The nature of superconductivity in thin films varies from that of the bulk. For external fields applied in-plane to a thin superconductive film, superconductivity is protected from the orbital effects of the in-plane field and thus extends to higher critical fields than for the bulk. In this case, superconductivity is broken by the alignment of paired electrons when the Zeeman energy is equal to the gap energy, or $\mu_B H_p \approx \Delta$, where μ_B is the Bohr magneton. Then the upper critical field is determined by the Pauli paramagnetic limit, $H_p(T = 0) = 1.86 T_{c0}$, in units of Tesla. Also known as the Chandrasekhar-Clogston limit [55], [56], this enhancement is attributed to the dimensional restraint on the formation of vortex cores in thin films [16], [34], [57].

It then follows that an unconventional superconductor is one that cannot be completely described by the BCS theory of superconductivity and whose Cooper pairs are bound by an exchange mechanism other than phonon-electron interactions. A new type of unconventional superconductivity emerged in 2015 with a publication by Lu *et. al* demonstrating an in-plane critical field well above the Pauli paramagnetic limit in gated MoS_2, which has similar properties to $NbSe_2$ [16]. The Pauli paramagnetic limit can be exceeded in cases where spin-triplet pairing occurs from strong spin-orbit

coupling. This is the case for Ising superconductivity, the predicted mechanism of superconductivity for NbSe$_2$ [34].

3.2.2 2H-NbSe$_2$

2H-NbSe$_2$ is a metallic TMD with trigonal prismatic structure [35]. Owing to advances in mono- and few-layer isolation of layered materials, studies of thin NbSe$_2$ have attracted newfound interest. In monolayer NbSe$_2$, an enhancement of the charge density wave transition temperature has been observed together with the superconducting phase [58]. NbSe$_2$ is a type II superconductor with a bulk transition temperature of ~7.2 K. Below 7 layers, the transition temperature of NbSe$_2$ decreases with decreasing dimensionality, where the transition temperature for monolayer NbSe$_2$ occurs instead ~3 K [17], as shown in Figure 6a. Figure 6b shows the sustained superconductivity above the Pauli paramagnetic limit in few layer NbSe$_2$ as a result of Ising SOC, and its thickness dependence [34].
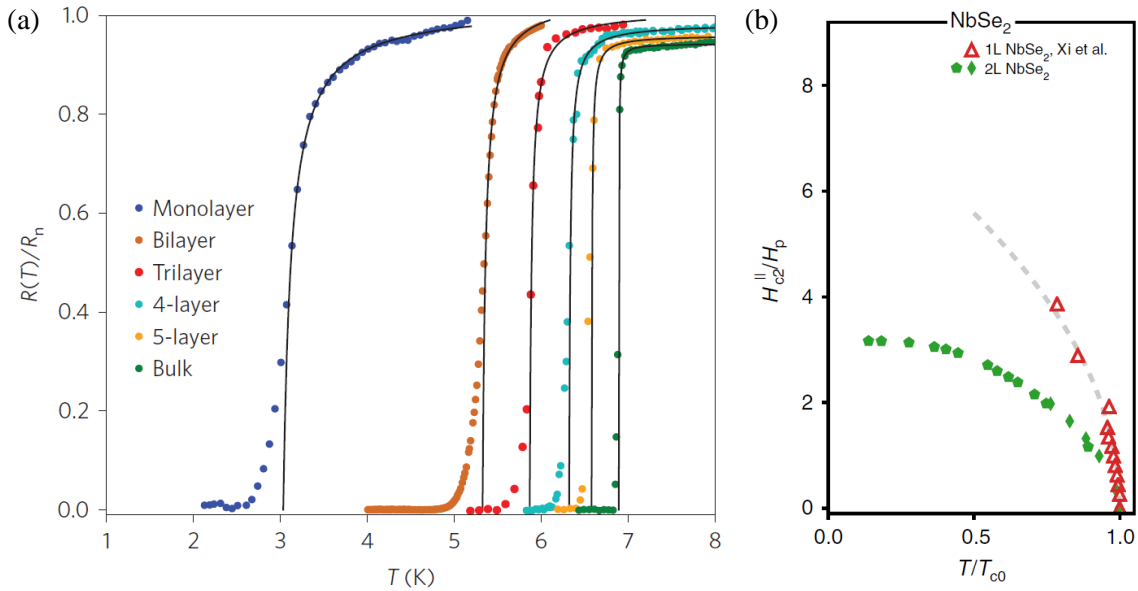
Figure 6: a) NbSe$_2$ thickness dependence of T$_c$ [17]; b) H$_{c2}$ enhancement in NbSe$_2$ [34].

NbSe$_2$ has broken in-plane mirror symmetry and strong SOC owing to the *4d* orbitals in niobium. Due to time reversal symmetry and spin orbit interactions, electrons near the $\pm$ K valleys experience strong and oppositely polarized Zeeman fields that result in spin-valley locking. These effective Zeeman fields pin the electrons in the out-of-plane direction such that the spin polarization is opposite for opposite valleys. This is notably distinct from 2D Rashba SOC which pins electron spins to the in-plane directions [33]. The strong pinning of the electrons through spin-valley locking inhibits spin

14

alignment (and hence pair breaking) from an in-plane external magnetic field. This, in combination with weak interlayer coupling, results in an enhanced in-plane H_{c2} above the Pauli limit and is the defining nature of an Ising superconductor. In a conventional superconductor, an external magnetic field will quench superconductivity due to orbital effects (vortex formation) and spin alignment that breaks Cooper pairs. In the 2D limit, interlayer coupling is minimized, and orbital effects negated. For an Ising superconductor, the in-plane upper critical field is given by $H_{c2}^{\parallel} \sim \sqrt{H_{SO}H_p}$, where $H_{SO} = \frac{\Delta_{SO}}{\mu_B}$ and Δ_{SO} originates from the SOC. Strong SOC where $H_{SO} \gg H_p$ results in an upper critical field well above the Pauli limit. The opposite spin locking in the out-of-plane direction further allows both spin-singlet and spin-triplet Cooper pair mixing in Ising superconductors [17], [33], [34], [59]. For monolayer NbSe$_2$, the theoretical H_{c2} for an in-plane field is 35 T, and has been experimentally measured as ~31.5 T. This enhancement for monolayer NbSe$_2$ is a result of spin-orbit interaction effects for non-centrosymmetric superconductors [17].

Absent in the current literature of NbSe$_2$ and 2D Ising superconductors is a direct measurement of Ising superconductivity. To probe Ising pairing nature in NbSe$_2$, a spin polarized measurement of the material is necessary. This is traditionally achieved using ferromagnetic semi-metallic leads, however the spin polarization in this geometry is known to be weak. The arrival of 2D VDW magnets sheds light on this dilemma by enabling the fabrication of a superconducting spin filter tunnel junction with strong polarization to probe 2D NbSe$_2$ [36].

3.3 Spin Filter Tunnel Junctions

3.3.1 2D Magnets

Ferromagnetism refers to the alignment of spins, or magnetic moments, in a material to generate a permanent and uniform magnetic field [60]. In a three-dimensional (3D) system, this permanent magnetization is possible because of the long-range magnetic order in the material. The desire to understand magnetism with respect to dimension, and particular interest in 2D magnets, has existed for many years [61]. Advances in epitaxial growth techniques brought the search for 2D magnets closer, but this method is limited by the inevitable presence of defects in the grown films [62]. The discovery of graphene and progress in the exfoliation of VDW materials generated a new effort toward the isolation of a 2D magnet, however, it was more than ten years after the famous discovery of graphene in 2004 that the first true 2D magnet was realized [36]. The challenge arises from the

Mermin-Wagner theorem, which states that for 2D systems, thermal fluctuations suppress long-range magnetic order in the Heisenberg model [63]. Magnetic anisotropy overcomes this limit.

Magnetic anisotropy describes the preference of magnetization to align with a particular crystallographic direction in a material. Magnetocrystalline anisotropy is a result of spin orbit interactions and is thus intrinsic to the material [64]. Magnetocrystalline anisotropy is common among VDW magnets as a result of reduced crystal symmetry [36]. Some of these bulk materials additionally have 2D magnetic interactions, suggesting they may retain magnetism in their 2D form. This was demonstrated for several materials that were thinned down to a few layers, including chromium trihalides [37], $CrSiTe_3$ [65], and others [66], [67]. However, a true 2D magnet has magnetism even as an isolated monolayer. This was first demonstrated by Huang *et al.* in 2017 for monolayer CrI_3 [36].

3.3.2 Chromium Trihalides

The discovery of CrI_3 as a 2D magnet caused an eruption of research to further understand the properties of CrI_3 and the related chromium trihalides. 2D chromium trihalides are stable intrinsic ferromagnetic semiconductors that have a CrX_3 (X=Cl, Br, I) structure [37]. Monolayer chromium trihalides have indirect band gaps that are fully spin polarized in the same direction at the valence and conduction band edges. Owing to intrinsic magnetocrystalline anisotropy and large magnetic moments [37], [68], [69], chromium trihalides are being explored as candidates for spintronics applications.

From the chromium trihalide family, $CrBr_3$ has strong intralayer ferromagnetic coupling and stacks ferromagnetically in both its bulk and 2D forms [37], [52]. This is compared to the more famous material, CrI_3, which has antiferromagnetic ordering in its 2D form. The Curie temperature for $CrBr_3$ is reported at 47 K for the bulk [68], and 37 K for 2D flakes [37]. Since ferromagnetic coupling is desirable for spin filtering, $CrBr_3$ can be used as a spin filter in a tunnel junction geometry to inject aligned spins into the superconductor under an external in-plane magnetic field.
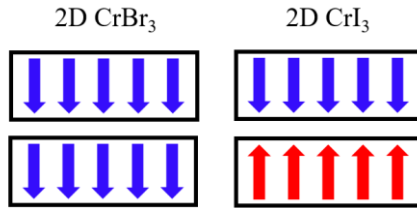
Figure 7: Ferromagnetic coupling in 2D CrBr$_3$ (left) as compared to antiferromagnetic coupling in 2D CrI$_3$ (right). Spin alignment in CrBr$_3$ is desirable for spin filter applications.

3.3.3 Spin Polarized Tunneling

Spin polarized tunneling, as the name suggests, refers to tunneling that is sensitive to spin polarization. Polarization in this context is defined as the difference in number of spin up and spin down electrons divided by the total number of electrons [70]. In the 1970's, Tedrow and Meservey studied thin superconducting tunnel junctions [71]. The resulting differential conductance, or tunneling conductance, at zero field showed a typical superconducting energy gap. For a metal counter electrode in an applied field parallel to the superconductor, the tunneling conductance is symmetrical, which indicates zero polarization or equal spin up and spin down strength. For a counter electrode that is a ferromagnet, the conductance becomes asymmetrical since the polarization is nonzero. The experiments by Tedrow and Meservey ultimately demonstrated that spin orientation is conserved in tunneling.
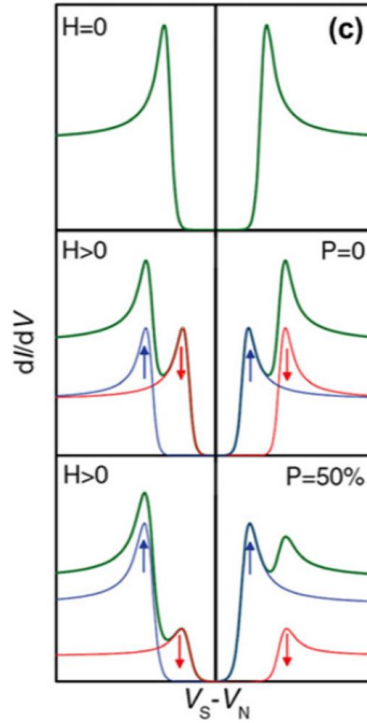
Figure 8: Conductance measurements demonstrating spin polarization [72].

A spin filter involves using a ferromagnetic insulating barrier in a tunnel junction geometry to generate a polarized current. The ferromagnetic barrier directly differentiates electron spins as oppose to symmetry filtering processes like those used to achieve giant tunnel magnetoresistance in devices [73]–[76]. The process works via exchange splitting causing a difference in tunnel barrier height for each spin polarization. A current-voltage measurement of a magnetic tunnel junction can be used to determine the extent of spin filtering [70], [74]. Hence, a superconducting spin filter tunnel junction consists of a ferromagnetic insulator sandwiched between a superconductor and a normal metal.

A superconducting tunnel junction operates on similar principles to a scanning tunneling microscopy probe. In other words, the differential conductance, $\frac{dI}{dV}$, in the low temperature limit is a direct measure of the density of states of the superconductor [77]. Using this principle with a spin filter geometry, it is possible to elucidate the pairing nature in the superconductor. For an Ising superconductor, which has both spin-singlet and spin-triplet pairing, a $\frac{dI}{dV}$ measurement with a sufficient spin filter can infer the relative occurrence of spin-triplet and spin-singlet pairing based on the measured polarization [71], [72], [74].

18

For the SFTJ device, the thickness of the CrBr$_3$ will affect the tunnel current and, by extension, the conductance. In work by Kim *et al.* [52], only bilayer CrBr$_3$ has a measurable conductance in a tunnel junction geometry at low voltage, as shown in Figure 9a. The SFTJ device must be biased in the range and on the order of the superconducting gap of NbSe$_2$, which is ~51 meV using a transition temperature of 7.2 K (Equation 1). Thicker CrBr$_3$ flakes have negligible conductance in this bias range, which is evident in the IV characteristics of an 8-layer CrBr$_3$ sample in Figure 9b.
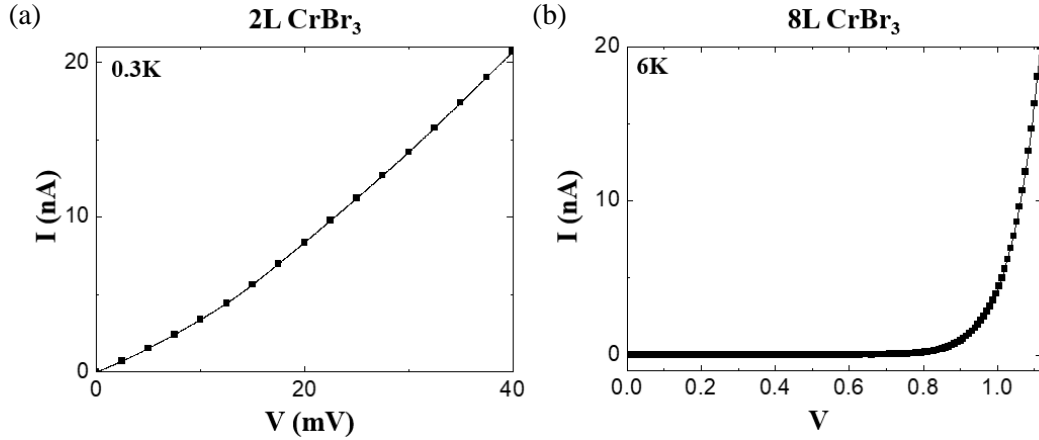
Figure 9: IV curve of a) bilayer CrBr$_3$ and b) 8-layer CrBr$_3$ [52].

3.3.4 Ising Superconductor Conductance Enhancement

According to Zhou *et. al* [33], Ising SOC allows the formation of spin-triplet Cooper pairs by electrons with equal spin polarization in the in-plane direction. They predict that a polarized half metal lead can tunnel Cooper pairs into the superconductor. Spin polarization in the half metal lead imposes a restriction on the injection of spin singlet pairs into the superconductor, resulting in a maximum (minimum) amplitude of Andreev reflection when the half metal lead is polarized to the in-plane (out-of-plane) direction. This can be explained by the behaviour of the device in magnetic fields. For a out-of-plane field, the pairing in the Ising superconductor is composed of oppositely aligned electrons, which means there is no spin selectivity. However, in an in-plane field, it is expected that the triplet pairing is composed solely of equal-spin electron pairs and spin-singlet injection is suppressed.
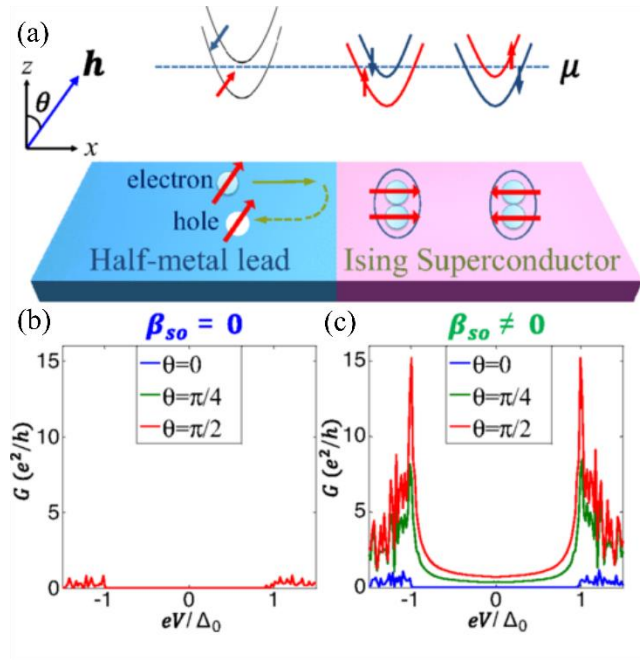
Figure 10: a) A half metal lead with spin polarization h in contact with an Ising superconductor whose spin-singlet and spin-triplet Cooper pairs have electron spins pointing to the in-plane directions; b) The tunneling conductance at a half-metal/Ising superconductor interface without SOC and c) with SOC. The tunneling conductance decreases when h deviates from the in-plane directions [33].

In a superconducting spin filter tunnel junction, a similar enhancement can be expected. Thus, for an $NbSe_2$-$CrBr_3$-Gr junction, where Gr is few-layer graphite, several features in conductance measurements are plausible. First, following the theory of spin polarized tunneling, the conductance peaks could be asymmetric under an externally applied in-plane field. From the asymmetry, the electron polarization can be determined. Second, according to the theory above regarding Ising superconductivity, an enhancement should also be present in an in-plane magnetic field from the tunneling of spin-triplet pairs.

3.4 Experimental Methods: NbSe$_2$ Device

3.4.1 Device Fabrication

A solution of 6 wt% poly(bisphenol A) carbonate (Sigma-Alderich 181635) in chloroform (Sigma Alderich 34854) is prepared by heating the mixture at 40 °C for ~2 hours with a magnetic stir bar until homogenous. Operating in a fume hood, a thin PC film is formed by pressing a few drops of the solution between two glass slides and sliding them apart, leaving a film on each slide. The slides are placed on a hotplate at 90 °C for 5-10 minutes to completely evaporate the chloroform from the surface after which they can be removed from the fume hood. Using a razor blade, the film is cut into squares ~5 mm in length. A square window ~ 2 mm in length is cut from a piece of tape that is used to pick up a square of PC. This window of PC is then gently placed on a ~1 mm square piece of PDMS on a glass slide. The PC window is fixed down by additional pieces of tape. It is important that the PDMS piece is very small so that the PC film does not delaminate from the PDMS during the pick-up process. The glass slide with the PC/PDMS is then affixed to the transfer stage.

All samples are exfoliated and transferred in a nitrogen filled glovebox. Flakes are selected according to their optical contrast on silicon. The silicon ships are cleaned with acetone and then isopropanol (IPA) for 5 minutes each by sonication, then blown dry with nitrogen. CrBr$_3$ and Gr flakes are exfoliated on oxygen plasma treated substrates. The process of picking up a flake from Si/SiO$_2$ is described as follows. First the flake and PC are aligned to the desired position and the sample stage is heated to 40 °C. The PC is brought close to the substrate by first focusing on the substrate, then adjusting the focal plane to be slightly above the substrate, and then bringing the PC layer down to this new focal plane by manipulating the z-axis. This process is repeated as necessary, allowing for adjustments of the PC and flake positions, until the PC is just about to touch the substrate. The PC is then brought into contact, advancing manually as slowly as possible (< 1 µm/s), until it just covers the flake. The temperature is increased to ~120°C, and promptly reduced back to 40 °C. This brief instance at high temperature ensures proper contact is made between the flake and the PC. Conformal contact of the PC with the substrate occurs when there are no visible shadows along the outside edges of the flake(s). Once the temperature has reduced to 40 °C, the PC is very slowly lifted to pick up the flake. This process is repeated to pick up subsequent flakes, forming a stack. Note that the temperatures described above are optimized for the glass transition temperature of PC assuming perfect heat transfer from the stage to the sample. For a custom built heated transfer stage, these temperatures may require adjustments according to the position of the heater,

thermocouple, etc.. In our lab, starting and ending at 40 °C is acceptable, but heating to 120 °C is adjusted to 160 °C for picking up flakes.

5/40 nm Ti/Au electrodes are pre-patterned using standard photolithography methods. The stack is transferred to the pre-patterned electrodes by bringing the flakes into contact with the substrate at 40 °C, as described for the pick-up process. The stage temperature is increased to 160 °C or higher (200 °C in our lab), melting the PC which has a glass transition temperature of ~150 °C. Once melted, the glass slide is carefully raised, leaving behind the PC and the transferred flakes. Depending on the application, the PC film can be left on the device as an extra protective layer against oxidation. Chromium trihalides are notorious for degrading rapidly in air, even when encapsulated by hBN. Leaving the PC layer on significantly improves the lifetime of the device in ambient air. For alternative applications such as optical measurements, or to measure flake thickness by AFM, the film can be removed by gently dipping the substrate in chloroform and carefully drying it with nitrogen gas. The fabrication steps described above are used to fabricate the SFTJ device by first picking up hBN, then Gr, $CrBr_3$, $NbSe_2$, Gr, and a bottom hBN flake.

The fabrication of the SFTJ device with $NbSe_2$ and $CrBr_3$ requires careful consideration of geometry. First, the $NbSe_2$ should be thin enough to suppress the orbital effects of an out-of-plane external magnetic field. Monolayer $NbSe_2$ is ideal to achieve the greatest in-plane H_{c2} enhancement in Ising superconductors [33], [34], however, this is impractical for mechanical exfoliation. Since the interlayer interactions in $NbSe_2$ are weak, few layer $NbSe_2$ should still demonstrate an H_{c2} above the Pauli limit, and other associated phenomena [35]. As discussed earlier in Section 3.3.3, the $CrBr_3$ imposes a trade-off where a thicker flake provides better spin filtering, but exponentially reduces the tunneling current. The overlap area between the $CrBr_3$ and the $NbSe_2$ also imposes a trade-off for which a larger area is desirable to increase the tunneling current, but also increases the chances of including a defect or impurity in the $CrBr_3$ layer. This could cause shorting in the tunnel junction. Generally, a contact area ~1-2 μm^2 is ideal. Coincidentally, a large contact area is difficult to achieve anyway since thin $CrBr_3$ and $NbSe_2$ flakes tend to be quite small (with lengths averaging ~2-8 μm). Finally, it should be noted that even once a device is made and has been tested for shorts at room temperature, the flakes will still occasionally shift in the heterostructure. For a device with such a small overlap area, this is a detrimental effect and results in many shorted devices. After melting the PC, it is recommended to place the sample under vacuum for ~15-30 minutes.

22

The final device is shown in Figure 11. The PC was left on the device as a protective layer during measurements. Afterwards, it was removed in chloroform in order to measure the thickness of the $NbSe_2$ by AFM (Veeco AFM). From the AFM data, the thickness of the $NbSe_2$ is ~8-10 nm. A large particle (or possibly damage to the hBN) near the $NbSe_2$ was present after removing the PC. It may have affected the AFM measurement of the $NbSe_2$ thickness. However, from previous experience working with $NbSe_2$ and the fact that its optical contrast is similar to graphite, I estimate that the thickness is indeed ~10 nm. Further explanation is provided in Appendix A.
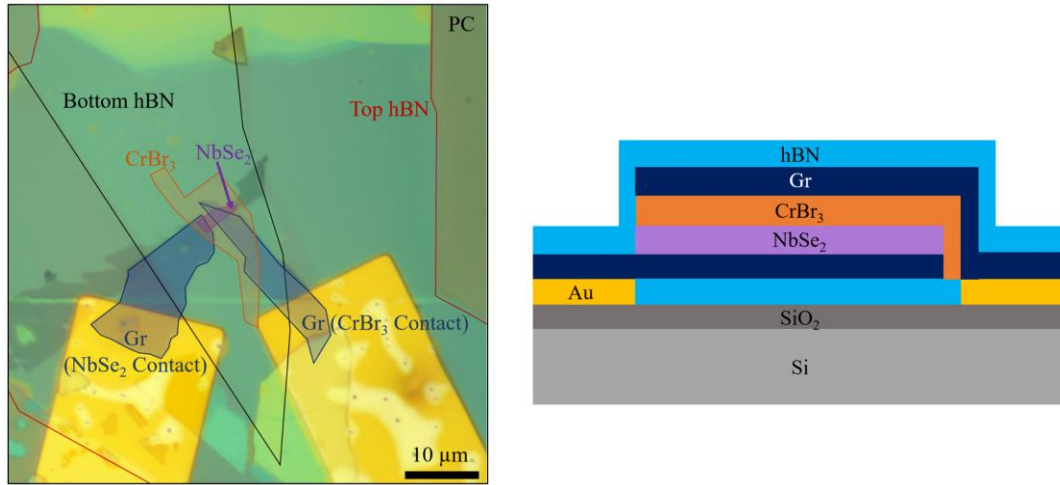
Figure 11: a) Fabricated SFTJ Device; b) SFTJ Schematic.

3.4.2 Tunneling Transport Measurements

The sample is loaded into a ^{3}He cryostat (Janis, base temperature 0.3 K). A piezo rotator (atto3DR) allows for precise rotation of the sample to the in-plane (~90°) and out-of-plane (~0°) orientations relative to the externally applied magnetic field. All measurements are performed at 1.4 K unless specified otherwise. The conductance is measured using lock-in techniques. A schematic is shown in Figure 12. A lock-in amplifier (Stanford Research Systems – Model SR830) supplies an AC voltage with an amplitude of 10 µV (77.777 Hz) to the sample, and also measures the conductance. The DC bias (Keithley – 2450 Source Meter) is swept between ±10 mV. A voltage divider configuration achieves these small applied biases without exceeding the accuracy of the instruments.
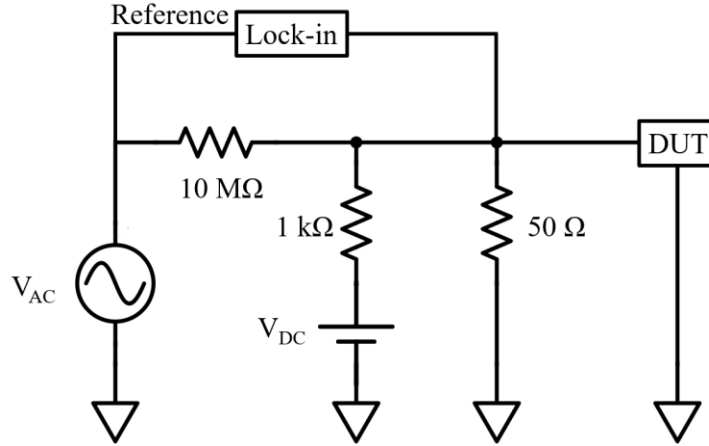
Figure 12: Tunneling conductance measurement setup.

3.5 Results

3.5.1 Characterization of NbSe$_2$

The superconducting nature of the NbSe$_2$ in the junction is examined first. Measurements at 0.3 K and 1.4 K show a superconducting gap of ~50 meV, with measurements at 1.4 K showing a more pronounced superconducting gap. This agrees well with the expected energy gap predicted by BCS theory, which is ~51 eV using Equation 1 and a transition temperature of 7.2 K. Unless specified otherwise, all measurements are conducted at 1.4 K and background subtracted using data taken at 9 K. As a result of this background subtraction, negative conductance values are plotted but should not be interpreted as the true measured conductance. Instead, the relative amplitudes of conductance curves are only considered in the data analysis. Figure 13a plots $\Delta(\frac{dI}{dV})$, which is the average difference between the height of the coherence peaks and the zero-bias conductance. As this value decreases and approaches zero, superconductivity is quenched. Referring to Figure 13a, the superconductivity in NbSe$_2$ is quenched above 7 K. From the work of Xi *et al.* [17], we can infer that the NbSe$_2$ flake is at least 7 layers thick based on this transition temperature. This corresponds with the measured AFM thickness of ~8-10 nm, which is ~9 layers (at 10 nm thick) of NbSe$_2$ assuming a monolayer thickness of 1.1 nm [78]. The superconductivity in NbSe$_2$ disappears similarly with the application of an out-of-plane magnetic field (perpendicular to the substrate), shown in Figure 13b, where the out-of-plane upper critical field occurs ~3-4 T.

24
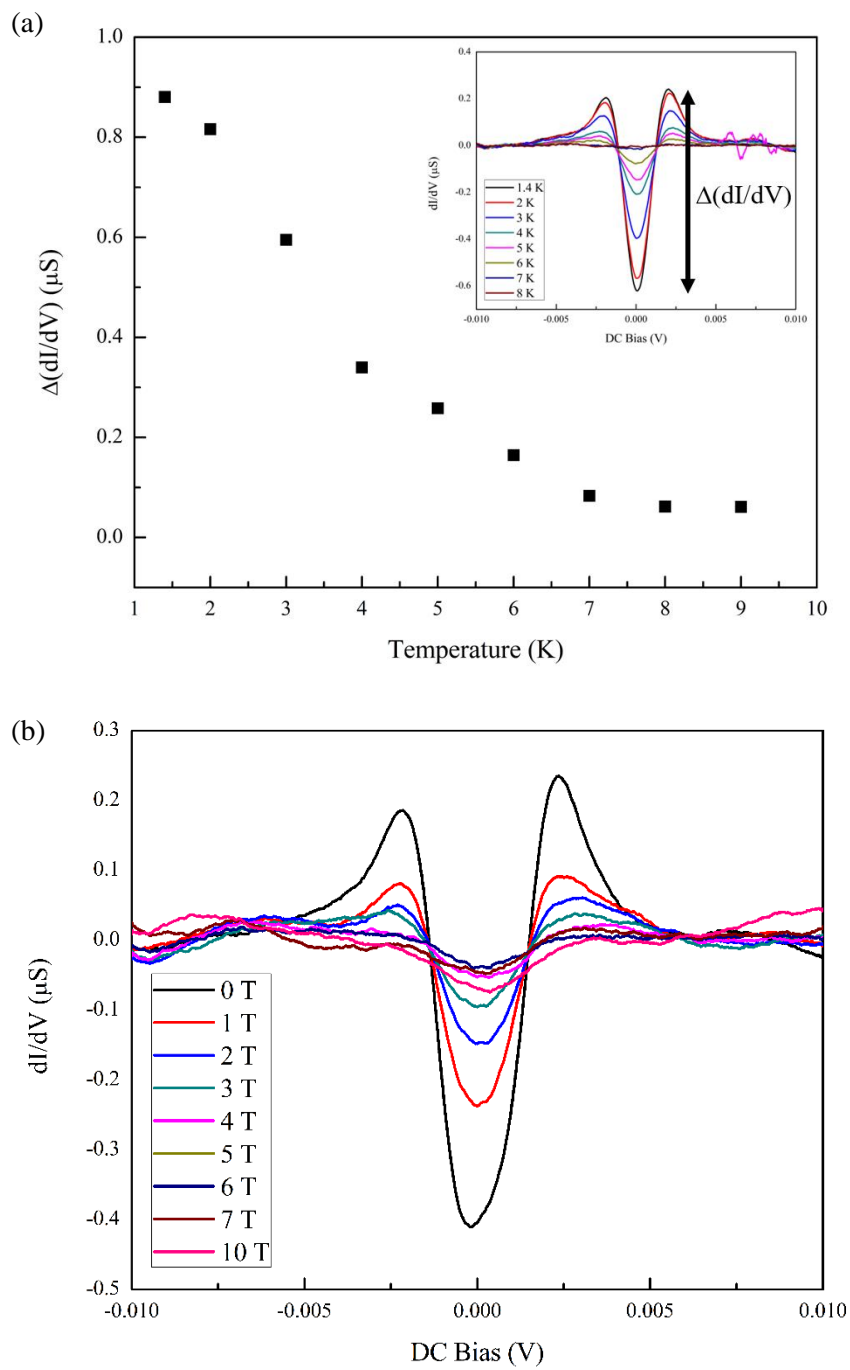
Figure 13: a) Temperature dependence, no background subtraction. Inset: background subtracted conductance curves; b) Effect of an external out-of-plane magnetic field.

3.5.2 In-plane Field Measurements

To determine the exact in-plane field angle of the system (parallel with substrate), the angle of the device was gradually changed to find the minimum zero-bias conductance, the results of which are shown in Figure 14. Since changing the angle of the sample stage generates heat (from the piezo motion, friction, and the voltage applied for the angle read-out), a stabilization period of ~2-3 minutes followed each adjustment. The resulting conductance versus time plot showed a series of steps that, when the noise of the angle changes was removed, depicted a clear minimum zero-bias conductance value indicating the precise angle where the sample experiences an entirely in-plane field. The offset between the ramp up and ramp down values is attributed to measurements on different days, and no background subtraction is used. Sweeping the angle up (85° to 96°) versus down generates a small hysteresis of ~1 degree.
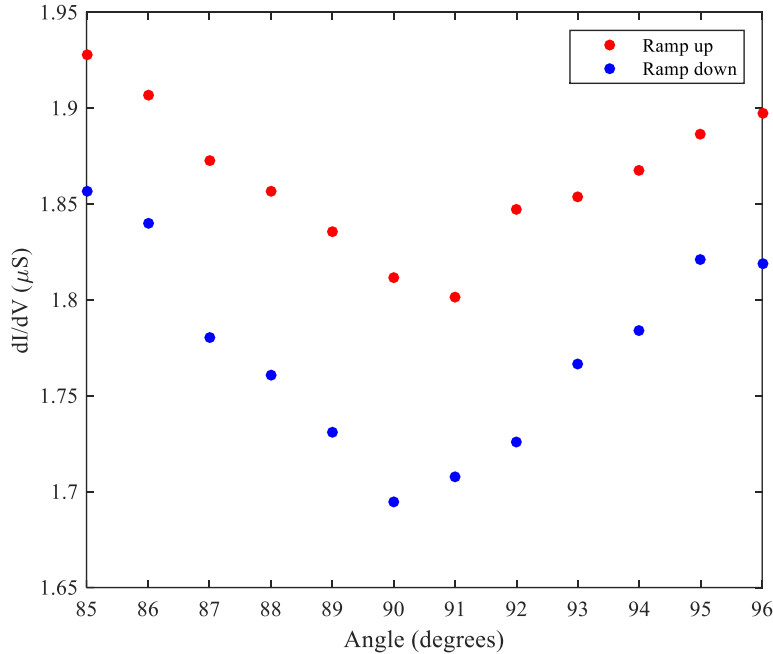
Figure 14: Angle dependence of the zero-bias conductance, no background subtraction. The minimum value corresponds to the precise in-plane orientation of the sample relative to an applied magnetic field.

With this information, a precise external in-plane field can be applied. The field was measured first from 0 T to 1 T, and then from 2 T to 10 T. There is no obvious enhancement or interesting change to the data with an increasing in-plane magnetic field. Between 0 T and 1 T, the superconductivity is

entirely unaffected. Between 0 to 10 T, there is a slight quenching of the superconductivity at higher fields, likely from in-plane orbital effects. This data confirms that $NbSe_2$ is an Ising system, since the in-plane field does not significantly quench the superconductivity from spin alignment effects.
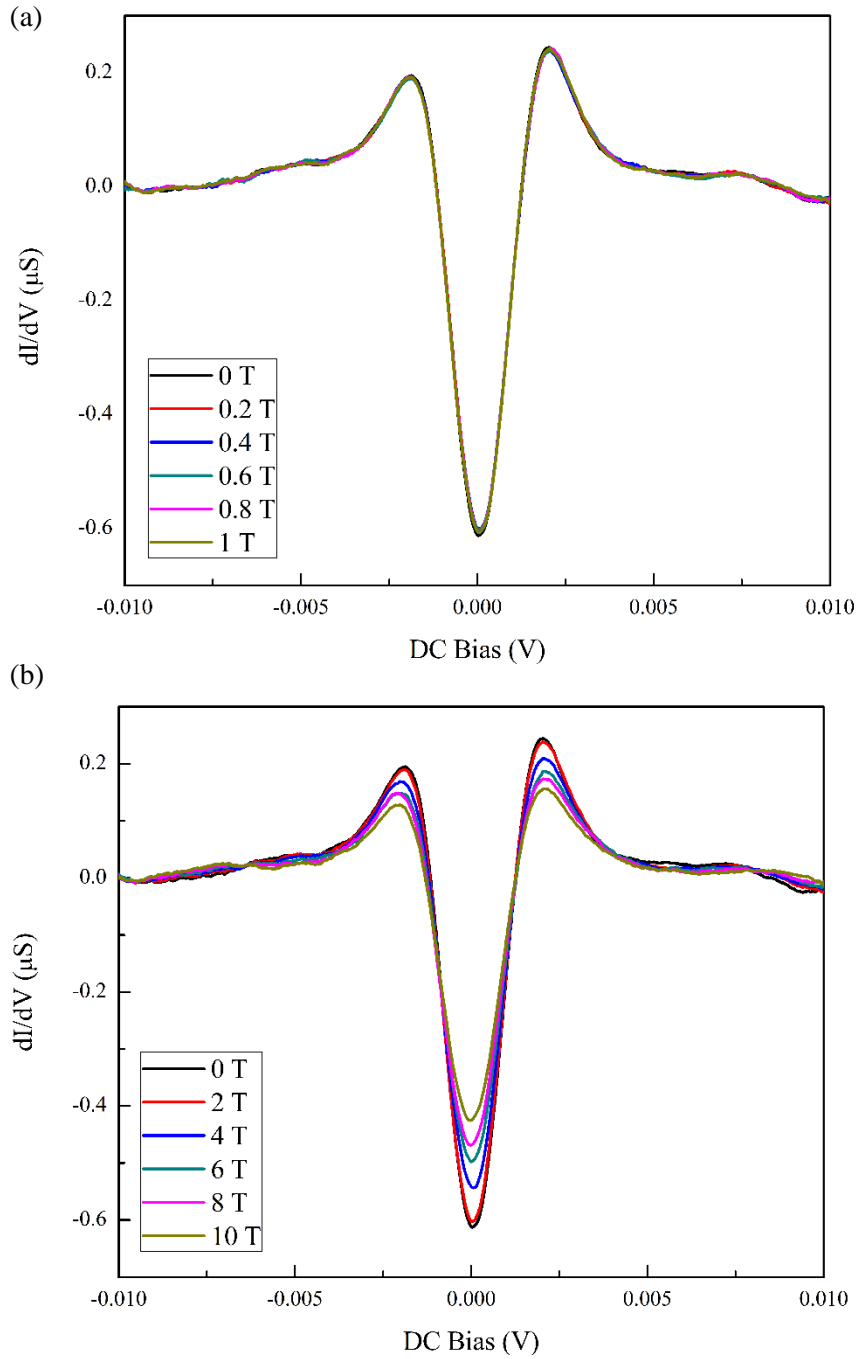
Figure 15: In-plane field dependence from a) 0 T to 1 T, and b) 0 T to 10 T.

To confirm if an enhancement for the in-plane field orientation is present, the sample was tilted at various angles (Θ) so that both in-plane ($B_\parallel$) and out-of-plane ($B_\perp$) field components are present in the applied magnetic field. The components are calculated using basic trigonometric relations. The sample is rotated back to an out-of-plane orientation ($B_\parallel = 0\ T$) and measured at the equivalent field components calculated from the angles. For example, if the sample is rotated to $\Theta = 30°$ with respect to the sample normal, and a 0.5 T external field is applied, then $B_\perp = 0.433$ T and $B_\parallel = 0.25$ T. The sample is rotated back to 0° and the field applied so that $B_\perp = 0.433$ T and $B_\parallel = 0$ T. If we assume an error on the same order as the hysteresis (~1-2°) observed in Figure 14, the effect on the field components is less than 5 mT and therefore negligible. The two measurements are compared by plotting $\Delta(\frac{dI}{dV})$ against the out-of-plane field components. Since both measurements have the same out-of-plane field component, the superconductivity suppression from vortices is equal. Therefore, if the $\Delta(\frac{dI}{dV})$ values for the $B_\parallel \neq 0$ T measurements are greater than the $B_\parallel = 0$ T measurements, an enhancement is present. The results of these measurements are shown in Figure 16. The conductance curves of these measurements can be found in Appendix B. In Figure 16, $\Delta(\frac{dI}{dV})$ is higher for all measurements containing an in-plane field component ($B_\parallel \neq 0$) which indicates an enhancement. A consistent ~1% enhancement of the zero-bias conductance is present, but it is too small for any further inferences to be made from the data concerning spin polarization. This does, however, confirm again that the NbSe$_2$ flake has 2D Ising superconductivity, and aligns with the prediction of Zhou *et al.* [33], save for the fact that the enhancement is much smaller than predicted.
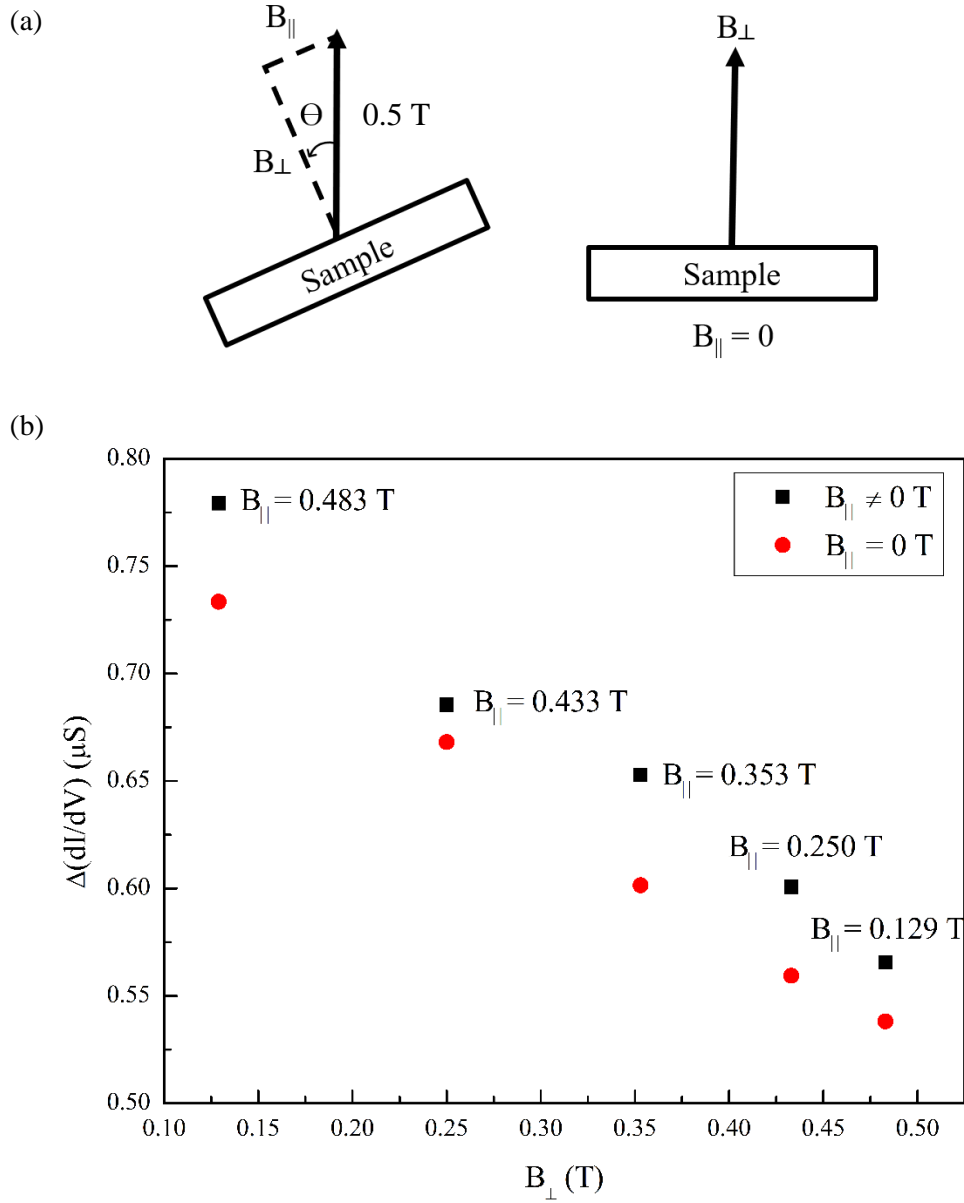
Figure 16: a) Left: Sample is tilted by Θ in 0.5 T magnetic field, Right: Sample normal to B⊥ measured at the same $B_\perp$ component calculated from Θ; b) Zero-bias conductance plotted for $B_\parallel = 0$ and $B_\parallel \neq 0$.

3.6 Discussion

There are perhaps two explanations for the absence of a large enhancement of the conductance in an in-plane magnetic field. First, it could mean that the $NbSe_2$ is too thick. The interlayer interactions of $NbSe_2$ are considered negligible, and $NbSe_2$ locally breaks inversion symmetry (regardless of layer number), but thinner $NbSe_2$ flakes closer to the monolayer limit may yield a greater conductance enhancement in an in-plane magnetic field. The theory by Zhou *et al.* is also given for monolayer $NbSe_2$, and the band structure of $NbSe_2$ does change with increasing layer thickness [79]. A higher quality device may also yield a more ideal superconducting gap, i.e. one where the zero-bias conductance drops to zero conductance. In general, it would be ideal to be able to measure the transport properties of the $NbSe_2$ flake directly with several electrodes on the flake. However, the geometry restrictions in the device fabrication usually limits the measurements to a tunneling geometry only, with only one electrode to choose from on each side of the junction. If the electrical contact is not ideal or some other phenomenon is occurring, there are no alternative measurement geometries to use as a comparison mainly due to difficultly in the fabrication. To understand the nature of the junction contacts, and to better characterize the asymmetry of future devices, IV measurements should be done. Another consideration that could be considered is the effect of switching the leads.

Also evident in the measurements is a lack of spin polarization. While there does appear to be a slight asymmetry to the conductance peaks, this asymmetry is matched by the 0 T in-plane field data (Figure 15) suggesting that it is simply intrinsic to the measurement. This, combined with the meager enhancement for in-plane magnetic fields, means that the $CrBr_3$ layer is likely not a sufficient spin filter. There is possible evidence that bilayer $CrBr_3$ does not demonstrate spin filtering based on different tunneling regimes. The reader is directed to the work of Kim *et al.* for more information [52]. The natural solution is to use a thicker $CrBr_3$ layer (e.g. trilyaer or 4-layer), but this may result in a negligible conductance due to an exponential decrease in tunneling current. If not, a different 2D spin filter material is necessary to achieve a spin polarized measurement of the pairing nature in $NbSe_2$, using the thinnest possible $NbSe_2$. Future work related to this type of measurement could see 2D chromium trihalides used in superconducting spin filter tunnel junctions that use other superconducting materials with compatible voltage requirements.

Chapter 4

Broadband Impulsive Vibrational Spectroscopy of 2D 1T′-MoTe$_2$

4.1 Overview: Orthorhombic MoTe$_2$

Bulk 1T′-MoTe$_2$ can be synthesized by growth methods. This material undergoes a transition from the monoclinic 1T′ (β) phase to the orthorhombic T$_d$ (γ) phase when it is cooled below 250 K (Figure 17b) [39]. Figure 17a shows the crystalline structure of the two phases, where the *ab*-plane is aligned with the layers and the *c*-axis is normal to the stacking direction of layers. The orthorhombic phase, which has broken inversion symmetry, has garnered significant interest since it is a candidate type II Weyl semimetal (WSM). A type II Weyl node is a contact point between the electron and hole pockets in the Fermi surface. Unlike Dirac points, such as in the graphene band structure, these 3D crossings are robust against small perturbations. This unique band structure is expected to manifest in exotic quantum transport behaviour [12], [13], [38].

Due to its candidacy as a Type II Weyl semimetal, a greater understanding of T$_d$-MoTe$_2$ and the transition between 1T′- and T$_d$-MoTe$_2$ is desired. Integral to the experiment is the fact that Raman spectroscopy is a proven effective probe of the two MoTe$_2$ phases. In this thesis, broadband femtosecond transient absorption (bb-fs-TA) spectroscopy is used to characterize the two phases of interest in MoTe$_2$. Using this technique, the transient absorption is measured after excitation of vibrational Raman modes in the sample. Some of the characteristic vibrational Raman modes can be observed and directly compared to Raman spectroscopy data. Similarly, the dynamics following excitation of the sample can be monitored and theoretically used to track the transition between the T$_d$- and 1T′- phases of MoTe$_2$. A photo-induced transition may be possible because of the strong phonon-electron coupling present in MoTe$_2$ [80].
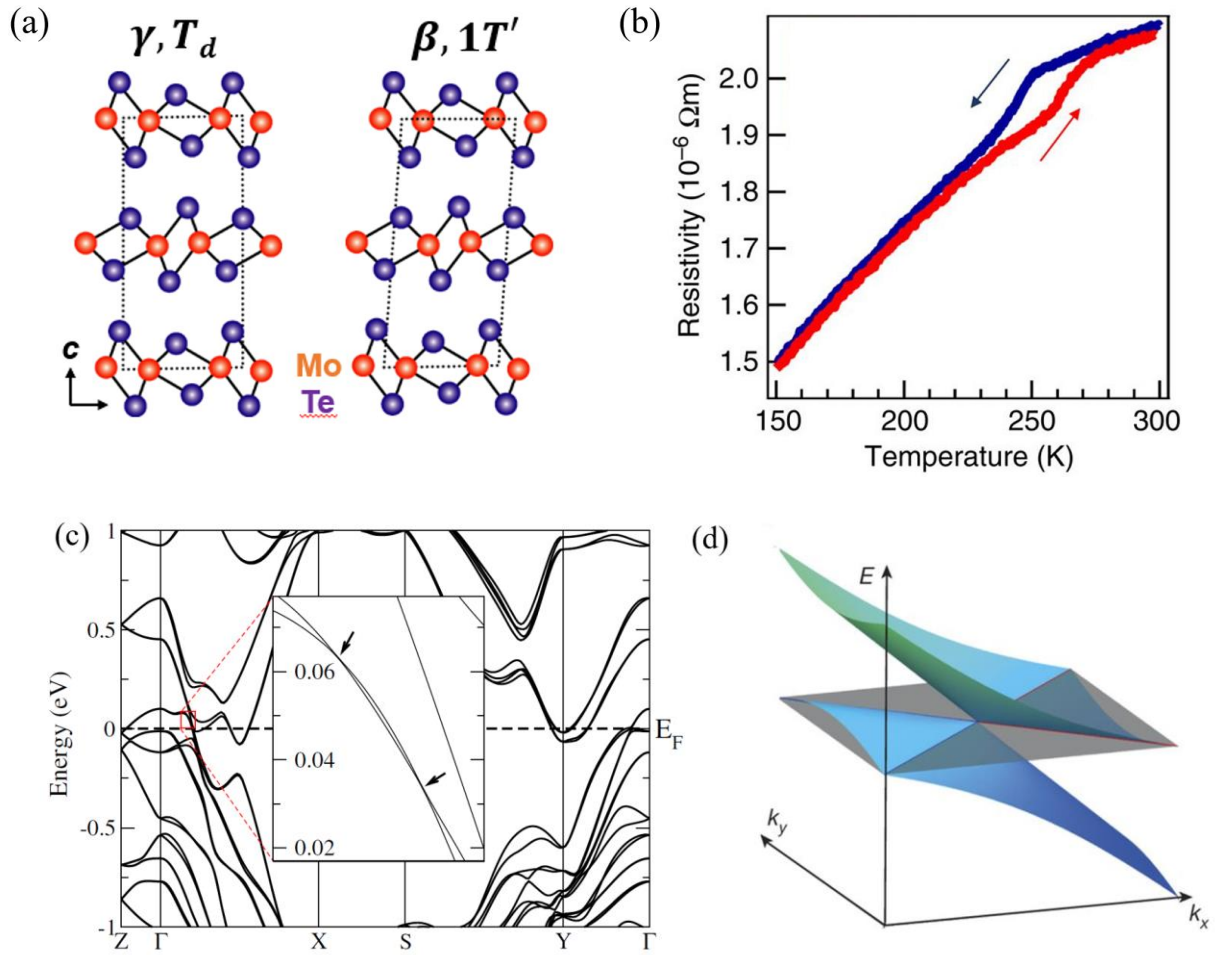
Figure 17: a) Orthorhombic (left) and monoclinic (right) phases of MoTe₂ [81]; b) Bulk resistivity of 1T′-MoTe₂ demonstrating reversible temperature induced phase transition to T_d-MoTe₂ [39]; c) Band structure of MoTe₂ with SOC showing band crossings [13]; d) Schematic of a type-II Weyl node [38].

4.2 Experimental Methods: MoTe$_2$ Devices

4.2.1 MoTe$_2$ Sample Fabrication

The samples are fabricated on silicon chips with a 25 nm or 50 nm silicon nitride (Si$_3$N$_4$) layer deposited layer on both sides. Standard photolithography methods are used to define etching areas on the wafer backside. Reactive ion etching removes exposed silicon nitride. The Si wafer is back-etched using KOH to form the silicon nitride window on which MoTe$_2$ is transferred. The result is shown in Figure 18a. For chips that accommodate transport measurements, a 100 nm Si$_3$N$_4$ layer is used and gold electrodes (Ti/Au 5/35 nm) are patterned using standard photolithography techniques. 1T′-MoTe$_2$ flakes were mechanically exfoliated and transferred to the chips using PDMS (Gel-Pak X4), and then covered with hBN for protection from oxidation. The thickness of the MoTe$_2$ is measured using AFM. Figure 18b-c show representative samples made on both types of chip design.
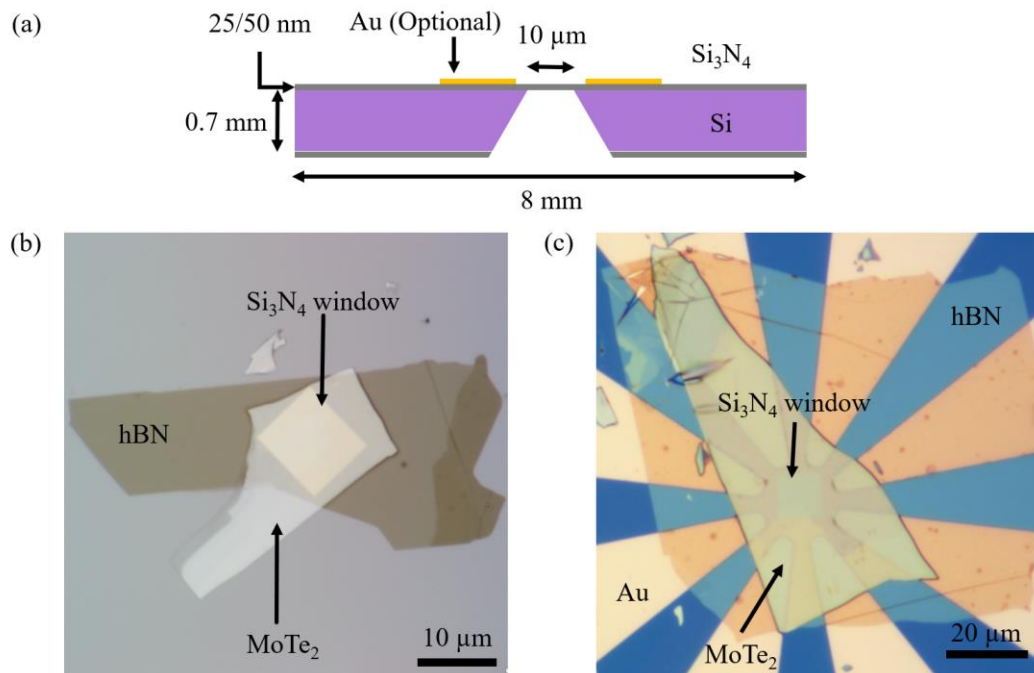
Figure 18: a) Chip schematic; b) hBN capped 38 nm thick MoTe$_2$ sample on Si$_3$N$_4$ window; c) hBN capped 40 nm MoTe$_2$ sample on Si$_3$N$_4$ window and surrounding electrodes.

4.2.2 Transient Absorption Measurements

Figure 19 shows a diagram of the optical setup used to collect transient absorption (TA) spectra. The MoTe$_2$ samples are mounted in an optical cryostat (Oxford Instruments, Optistat CF-V2) in vacuum with temperature control between 77 K and 500 K. Once equilibrated, the temperature is maintained within ± 0.01 K. Transient absorption (TA) spectra are collected using a synchronized dispersive spectrometer. A Light Conversion Pharos-6W amplifier is the light source that provides 180 fs pulses centered at 1030 nm (300 µJ, 20 kHz repetition rate). A broadband probe pulse with a range of 550 nm to 950 nm is created by focussing the beam into a 3 mm YAG window using 50 mm focal length lens, then passed through a short pass filter (Thorlabs FESH0950) to prevent saturation on the spectrometer, and finally collimated by an off-axis parabolic mirror. 520 nm (up to 10 µJ) pump pulses are generated by optical parametric amplification (OPA, ORPHEUS) followed by second harmonic generation (LYRA), with a spot size of 350 µm. The pump and probe pulses are focused onto the sample using 400 mm and 50 mm focal length lenses, respectively. The incident beams are both horizontally polarized and have a 10° angle between them. Room temperature measurements use a repetition rate of 1 kHz to prevent sample damage. Differential TA spectra are recorded as a function of pump-probe time delay (DS in Figure 19) using a mechanical chopper at 50 Hz to modulate the pump beam.
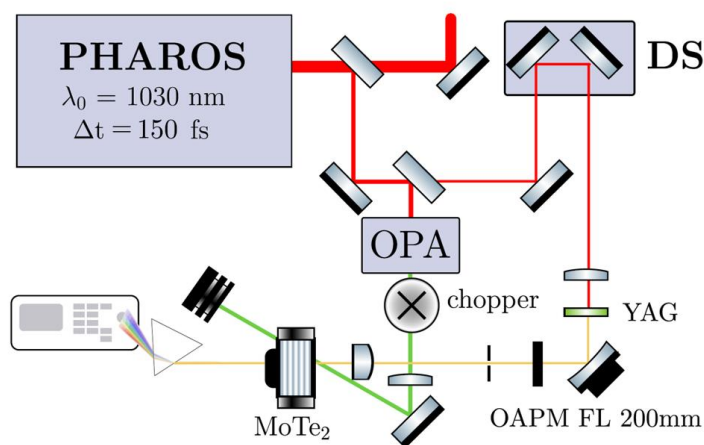
Figure 19: Optical setup for collecting transient absorption spectra.

4.2.3 Data Processing

Broadband femtosecond transient absorption (bb-fs-TA) is measured with respect to time delay with a time step of 30 fs. Figure 20a shows the chirp corrected TA, where the vertical line indicates time zero. A cross section at 2.0 eV (horizontal line in Figure 20a) yield the curve in Figure 20b. This is fitted with a sum of exponentials convoluted with a gaussian instrument response of 100 fs (FWHM). Electronic background subtraction is achieved by subtracting the fit from the normalized TA to produce the residuals in Figure 20c. A Fast Fourier Transform (FFT) analysis across all probe energies yields the phonon power spectrum in Figure 20d. Relative amplitudes of the observed frequency modes are extracted from energy cross-sections of this spectrum. The dynamics of the system are extracted by using a Continuous Wavelet Tranform (CWT) instead of an FFT to achieve time-resolved amplitudes of the frequency modes. The CWT is a method with good resolution in both the time and frequency domains [82]. The same corrections shown in Figure 20a-c are applied prior to applying the CWT. The resulting CWT spectrum is shown in Figure 20e. Energy cross-sections are averaged where the phonon mode amplitudes are strongest to acquire a high signal-to-noise ratio to yield time-dependent frequency mode amplitudes.
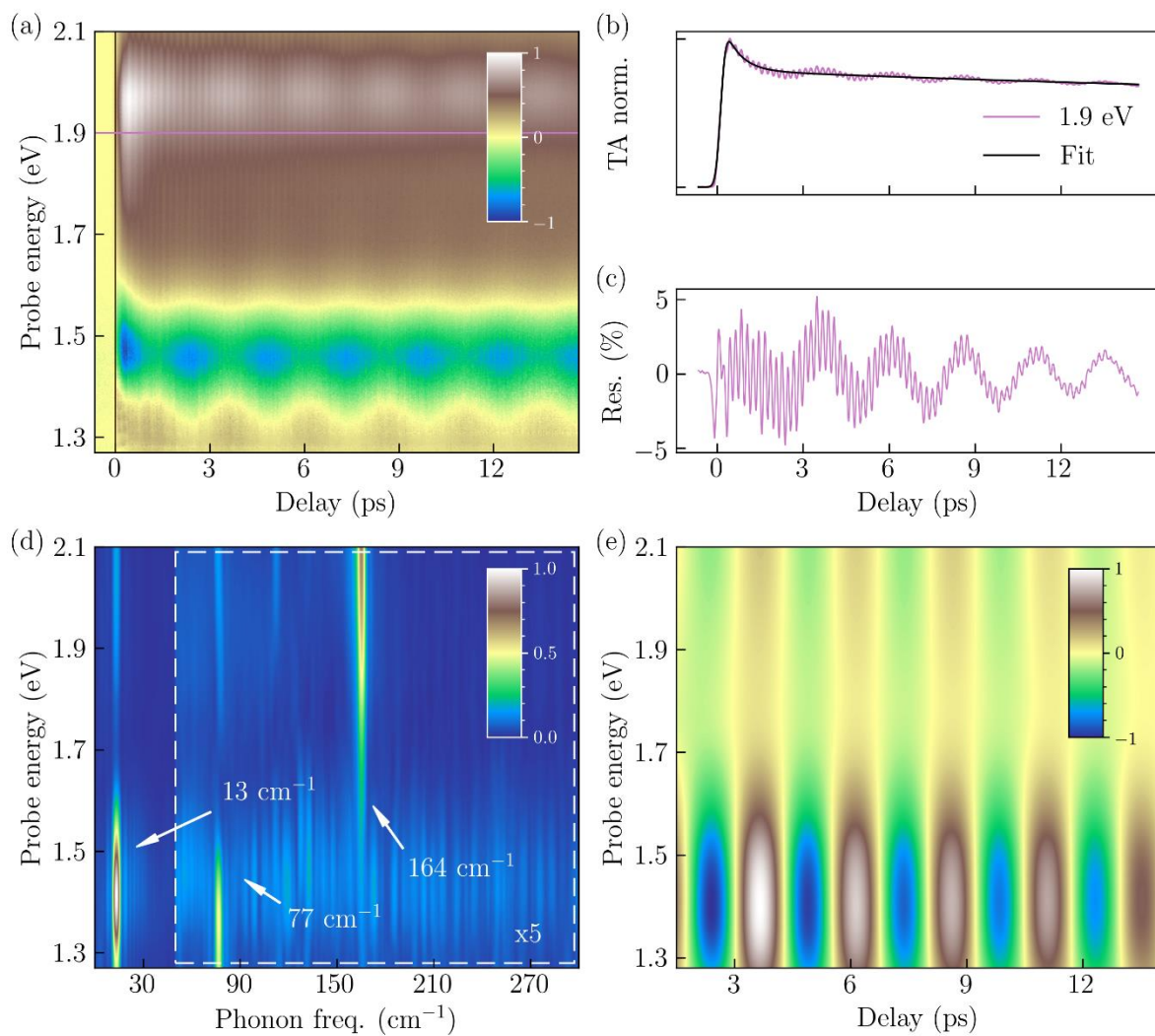
**Figure 20: 40 nm thick 1T′-MoTe₂ at 230 K. a) Chirp corrected bb-fs-TA; b) Cross-section at 2.0 eV and fit; c) Residual after electronic background subtraction (fit from b); d) FFT spectrum across probe energy range; e) CWT spectrum for 13 cm⁻¹.**

4.2.4 Magnetotransport Measurements

A 40 nm 1T′-MoTe$_2$ flake is used for the transport measurements. The sample is loaded in a ^{3}He cryostat (Janis) and measured at base temperature (0.3 K). Magnetic field measurements up to 12 T use fields in a perpendicular orientation with respect to the MoTe$_2$ *ab*-plane. The sample is first measured in the ^{3}He, then measured by bb-fs-TA spectroscopy at varying fluences, followed by additional transport and optical measurements to characterize any optically induced structural changes to the sample.

4.3 Broadband Femtosecond Transient Absorption Measurements

Femtosecond broadband transient absorption measurements characterize the vibrational frequency modes of 1T′- and T$_d$-MoTe$_2$ of varying thickness, as well as the dynamics of the transition between them. In the pump-probe scheme, the 520 nm pump pulse impulsively excites vibrational modes in the MoTe$_2$. The white light probe pulse that follows measures the transient absorption and any associated dynamics. Using this technique, it is possible to extract the vibrational Raman modes of the MoTe$_2$ at ~13 cm^{-1}, ~77 cm^{-1} and ~164 cm^{-1}. Notably, Raman spectroscopy measurements from the literature indicate that the interlayer shear mode at ~13 cm^{-1} is only active in T$_d$-MoTe$_2$, thus providing a clear distinction between the two phases. Figure 21a shows the Raman modes of bulk MoTe$_2$ in the 1T′-phase (320 K, red) and the T$_d$-phase (80 K, blue). Figure 21b shows a temperature dependence of the phonon amplitudes from bb-fs-TA spectroscopy measurements on a 40 nm 1T′-MoTe$_2$ sample. The transition to the T$_d$-phase is evident by the appearance of the ~13 cm^{-1} mode below temperatures on 250 K, which is consistent with Raman spectrum of Figure 21a [39].

(a)

(b)
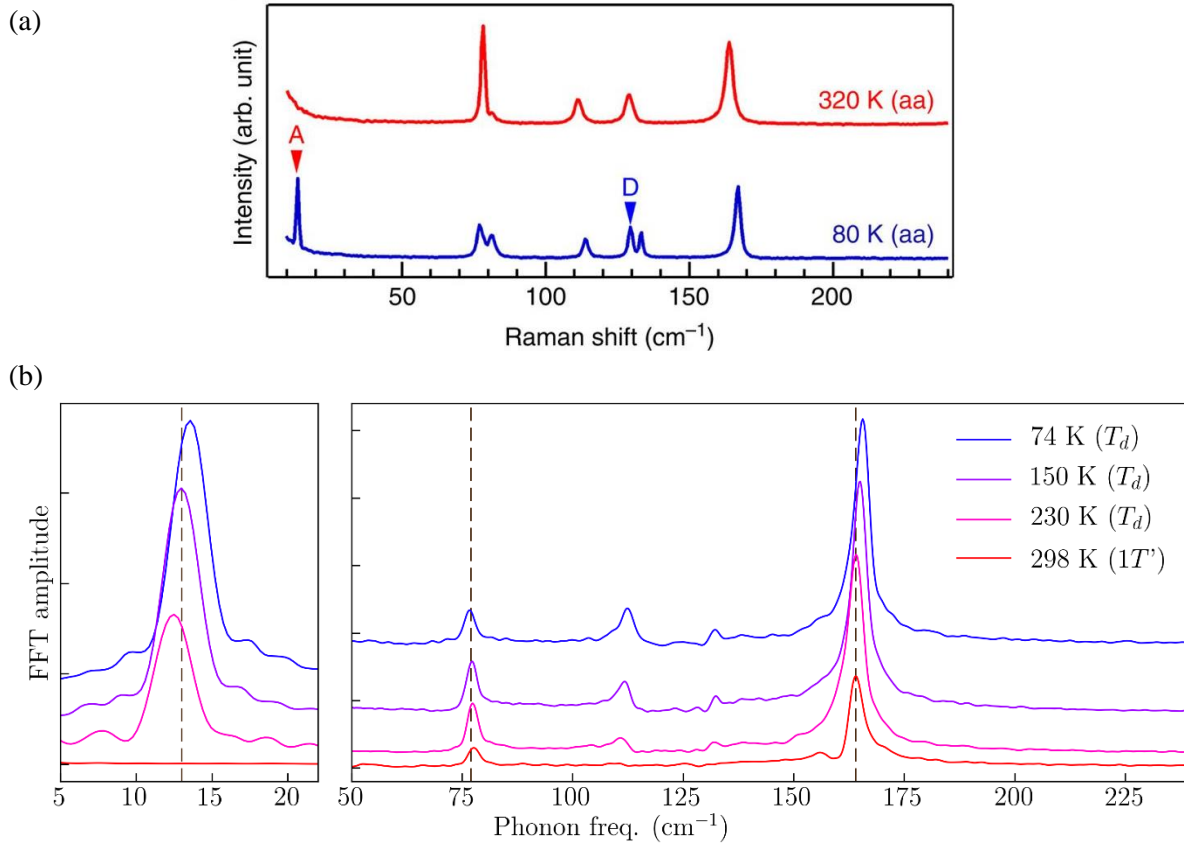
Figure 21: a) Raman modes of bulk 1T′-MoTe$_2$ at 320 K (1T′ phase, red) and 80 K (T$_d$ phase, blue) [39]; b) Temperature dependence of the phonon modes in a 40 nm 1T′-MoTe$_2$ sample.

Another avenue where the phase transition between the 1T′- and T$_d$-phases has been explored is through dimensionality. When 1T′-MoTe$_2$ is exfoliated to flakes thinner than ~12 nm, a transition to the T$_d$-phase is induced at room temperature (Figure 22b) [81]. Figure 22a shows the thickness dependence of the frequency modes as measured by bb-fs-TA spectroscopy. The data at low wavenumber includes a strong longitudinal acoustic phonon mode (~5-8 cm^{-1}) that interferes with the frequency mode at ~13 cm^{-1}. This diminishes the distinguishability between the two phases using bb-fs-TA measurements since the frequency modes at ~77 cm^{-1} and ~164 cm^{-1} provide little distinction between the two phases as compared to Raman spectroscopy measurements.

38
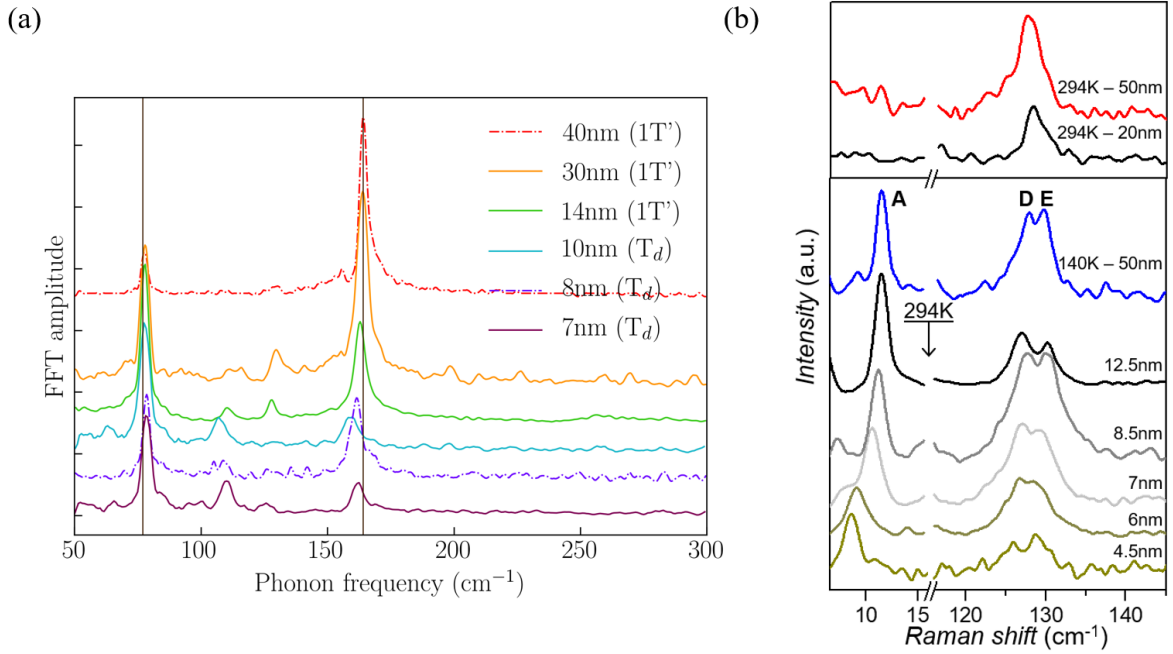
Figure 22: a) 40 nm MoTe₂ thickness dependence of phonon modes as measured by bb-fs-TA spectroscopy; b) Raman spectroscopy indicating a dimensionally induced phase transition from 1T′-MoTe₂ to T_d-MoTe₂ for flakes less than ~12 nm [81].

The phonon mode dynamics are extracted using a continuous wavelet transform (CWT). The resulting CWT intensities with respect to time are shown in Figure 23 for each frequency mode for a 40 nm sample at 230 K. The sample is irradiated with a fluence of 0.6 mJ·cm⁻², which corresponds to 60 K using the following formula:

$$\Delta T = \frac{F\,A\,M}{\rho\,C_p\,d},$$
(2)

where F is the fluence, A is the absorption (0.4 for 40 nm sample), M is the molar mass, C_p is the heat capacity, and d is the thickness of the sample. With the fluence stated above, the induced temperature change is ~60 K. The sample is at 230 K and therefore in the T_d-phase, but the 60 K of laser induced temperature should drive the sample to the 1T′-phase. If a phase transition occurs, then a discontinuity in the decay of the frequency modes is expected. The amplitude of the ~13 cm⁻¹ mode should also become zero. Evident in Figure 23, neither of these indicators appear, suggesting that a phase transition from the T_d-phase to the 1T′-phase has not occurred.
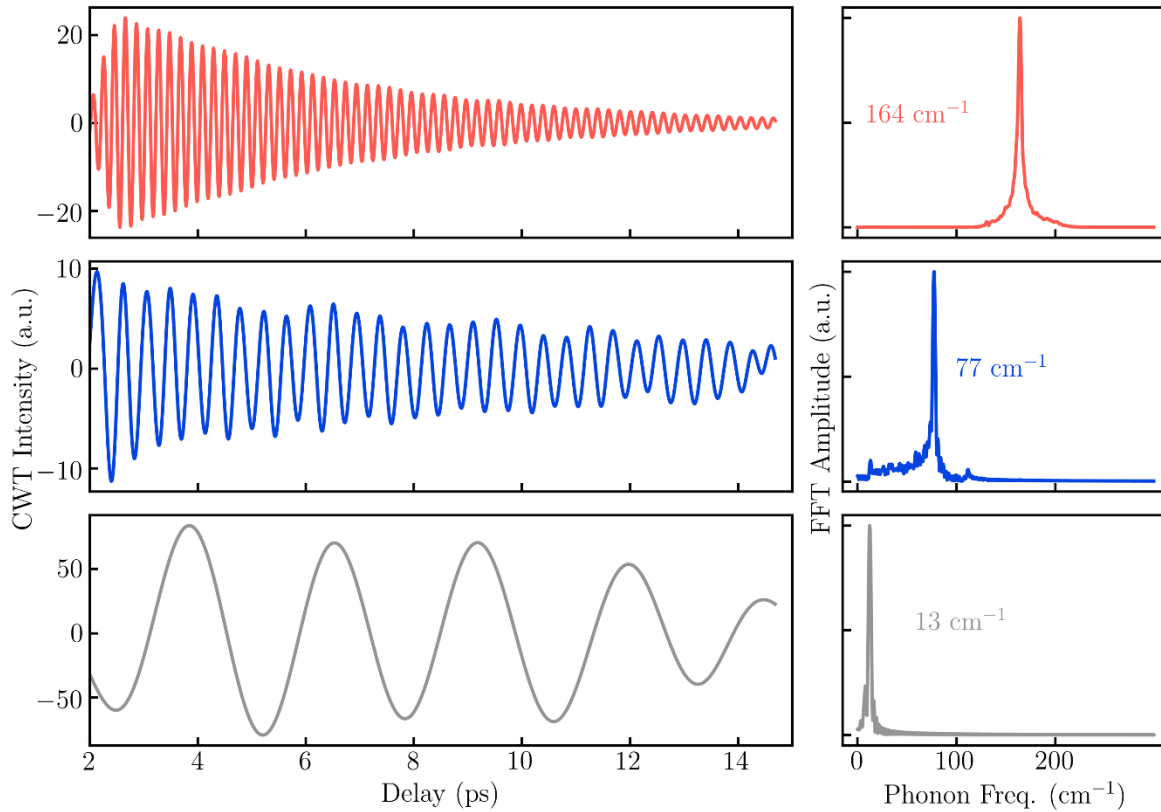
Figure 23: 40 nm sample at 230 K, irradiated with 0.6 mJ·cm⁻². CWT intensities with respect to time for the ~164 cm⁻¹ (top), ~77 cm⁻¹ (middle), and ~13 cm⁻¹ (bottom) frequency modes. Wavenumbers extracted by FFT shown on the right.

To further probe the behaviour of the system, the effect of fluence is measured on a 32 nm sample. The 40 nm sample degraded before this measurement could be done. Figure 24a shows the TA as a function of fluence on a 32 nm sample. A linear increase of the TA as the fluence increases is expected and indicates the sample has not been damaged. Figure 24b shows the FFT amplitude of the ~13 cm⁻¹, ~77 cm⁻¹, and ~164 cm⁻¹ frequency modes as a function of fluence. At fluences above 1 mJ·cm⁻², the FFT amplitude of the ~13 cm⁻¹ mode gradually diminishes to zero amplitude. Since the other frequency modes remain relatively unaffected and the transient absorption continues to increase linearly with the fluence, sample damage is not responsible for this effect. This result is suggestive of a transition to the 1T′-phase, whose Raman signature lacks the ~13 cm⁻¹ mode. This was demonstrated earlier with the temperature dependence of the frequency modes, however, there is reason to believe that this is not the case. First, the effect appears to be a permanent structural change.

Reducing the fluence does not recover the ~13 cm^{-1} FFT amplitude. Annealing the sample *in situ* at 500 K (diamond data points) and measurements at room temperature (inverted triangles) also fail to recover the sample properties at low fluence. These factors contradict the reversible nature of the temperature driven transition between the two phases.
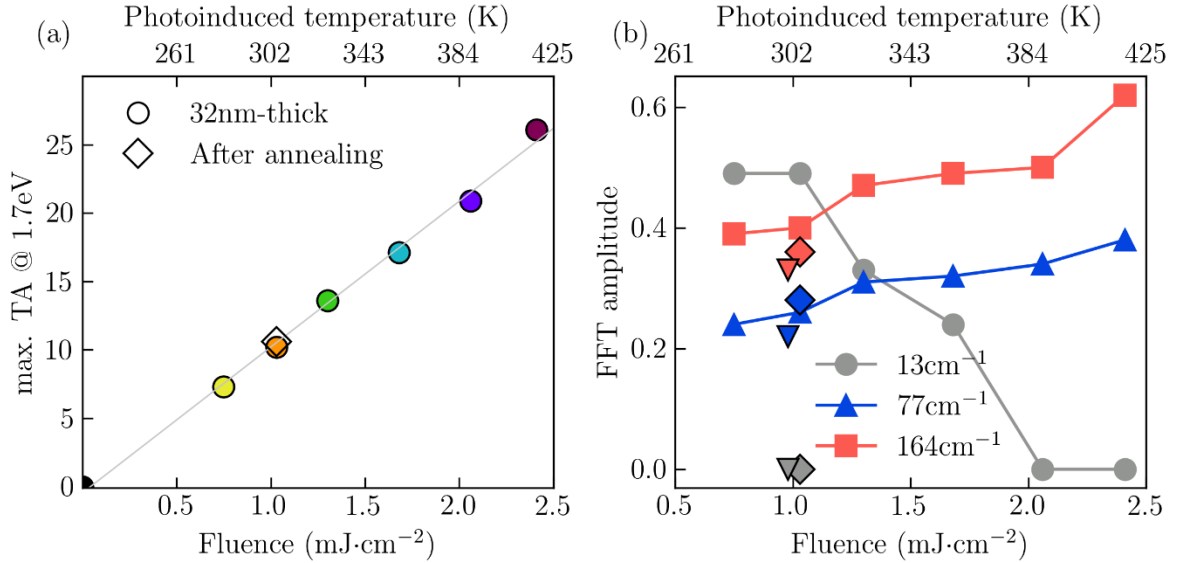
Figure 24: 32 nm MoTe$_2$ sample. a) Fluence dependence; b) FFT amplitude of the ~13 cm^{-1}, ~77 cm^{-1} and ~164 cm^{-1} frequency modes. Diamond data points represent values after annealing at 500 K. Inverted triangles are a 298 K measurement.

Finally, the decoherence of the sample does not correspond to the 1T′-phase. The coherent oscillations of each frequency mode experience some decay, with the ~164 cm^{-1} showing the most pronounced decay on the 15 ps time scale. As such, a time constant can be calculated from the dynamics of the ~164 cm^{-1} mode. The time constant, or damping time, is a measure of decoherence (dephasing) after the resonant impulsive excitation of the vibrational mode and is calculated at different temperatures with constant fluence of 0.6 mJ·cm^{-2} on the 40 nm sample. These results are shown in Figure 25. The vertical line intersects at 250 K, marking the transition temperature between T$_d$- and 1T′-MoTe$_2$. There are distinct damping times for each phase of MoTe$_2$, with 1T′-MoTe$_2$ demonstrating damping times above 6 ps compared to damping times less than 5.5 ps for the T$_d$-phase. The damping time decreases with increasing temperature, suggesting that thermal disorder may be causing faster dephasing. Calculating the damping times of the 32 nm sample at 220 K for each fluence yields values all below 4.5 ps which is characteristic of T$_d$-MoTe$_2$, not 1T′-MoTe$_2$.
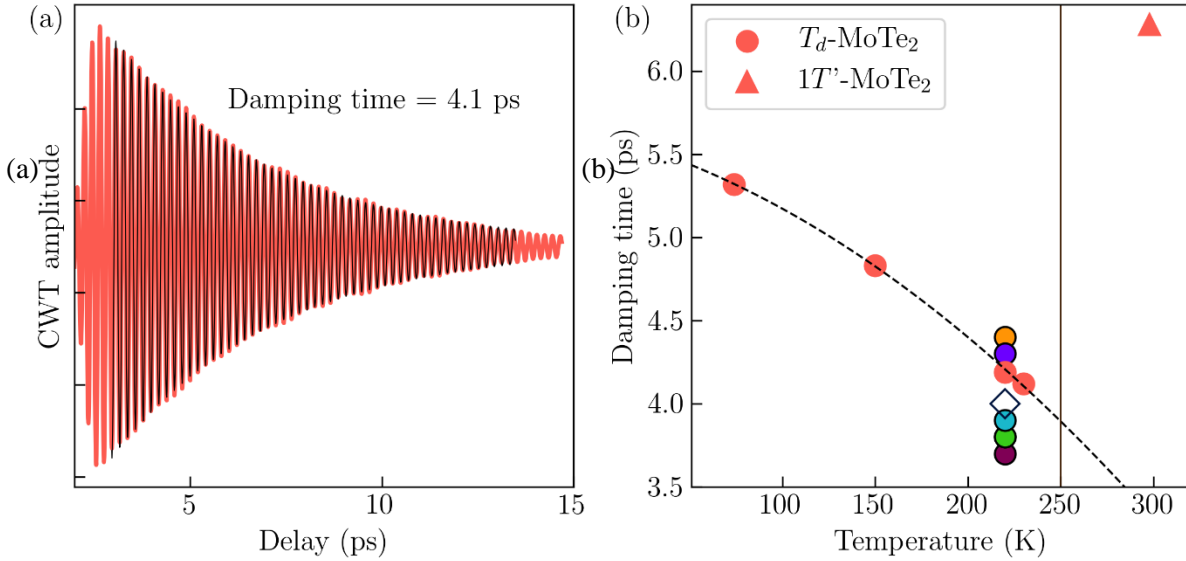
Figure 25: a) Time evolution of the 164 cm^{-1} mode amplitude for 40 nm MoTe$_2$; b) Temperature dependence of the damping times for 40 nm MoTe$_2$ sample. Damping times at different fluences for 32 nm MoTe$_2$ indicated by coloured circles corresponding with data points in Figure 24a.

This means that the sample structure features traits of both MoTe$_2$ phases: frequency mode amplitudes characteristic of 1T′-MoTe$_2$ and vibrational mode dynamics characteristic of T$_d$-MoTe$_2$. A light-induced structural change in the MoTe$_2$ has occurred. The apparent durability of this structural change, at least on a time scale of days, means that magnetotransport measurements are available to possibly corroborate the evidence of a structural change.

4.4 Magnetotransport Measurements

To fully characterize the structural change, magnetotransport measurements were done before and after irradiation at high fluences on a new sample. A 40 nm MoTe$_2$ flake is transferred to the chip such that the electrodes are approximately aligned with the *a* and *b* crystal axes (Figure 26). Current is sourced from three directions to account for anisotropy along different crystalline axes. This is shown in Figure 26a, where "*a*-source" is sourced along the *a*-axis, "*b*-source" is sourced along the *b*-axis, and "*ab*-source" is approximately 45° between the *a*- and *b*-axes. The longitudinal (ρ_{xx}) and transverse (ρ_{yx}) resistivities are measured for each orientation. These axes are labelled according to the magnetoresistance measurements (MR), discussed later in Figure 28. Previous literature indicates that the *a*-axis has the largest MR [83].

42

Oscillatory MR in high quality samples at high fields, termed Shubnikov-de Haas (SdH) oscillations, are a measure of the Fermi surface and have been observed in T_d-MoTe$_2$ [84]–[86]. Taking the FFT of the oscillations results in frequencies that correspond to electron and hole pockets. Therefore, a measure of the SdH oscillations in the MoTe$_2$ sample before and after irradiation can provide information on the electronic nature of the structural change. However, after irradiation no SdH oscillations are observed in the sample. The SdH oscillation measurements motivate measurements at 0.3 K. Since the SdH oscillations cannot be observed in the sample after irradiation, it is more logical to perform subsequent magnetotransport measurements at a temperature close to that which is used for the optical measurements, i.e. ~200 K. These measurements are currently in progress.
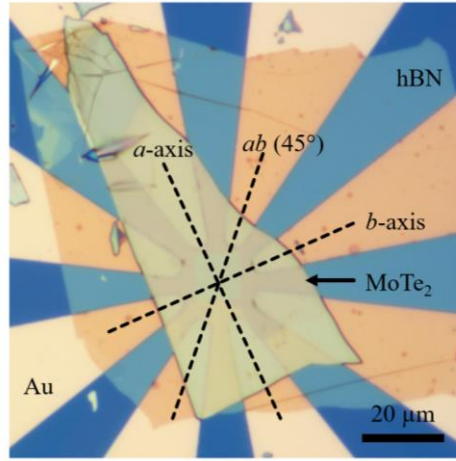
Figure 26: 40 nm 1T′-MoTe$_2$ flake prepared on a chip with a Si$_3$N$_4$ window and electrodes.

Figure 27a shows the transverse resistivity measurement before and after irradiation. Sourcing current along the *a*- and *b*-axis yields the same overlapping curve, indicating low anisotropy in the sample. After irradiation, the resistivity in the sample has a lower magnitude resistivity. Figure 27b shows the longitudinal resistivity before and after irradiation. Before the radiation, the residual resistivity (ρ_{xx} at zero field) is 0.919 µΩ·cm, 0.782 µΩ·cm, and 0.948 µΩ·cm for current sourced along the *a*-, *ab*-, and *b*- axes, respectively. These values increase to 14.3 µΩ·cm, 16.7 µΩ·cm, and 35.7 µΩ·cm, respectively, after irradiation. It has been shown for bulk MoTe$_2$ that giant MR and non-linear resistivity at low temperature is attributed to the compensation of electron and hole carriers [87]. The semiclassical two-band model assumes conduction by only one electron and hole pocket each [88], [89], and can be simultaneously fit to the resistivity curves to extract electron and hole carrier densities and mobilities. The field dependencies of the longitudinal and transverse resistivities are given by:

$$\rho_{xx}(B) = \frac{(n\mu_n + p\mu_p) + (n\mu_p + p\mu_n)\mu_n\mu_p B^2}{e\left[(n\mu_n + p\mu_p)^2 + (p-n)^2\mu_n^2\mu_p^2 B^2\right]}, \tag{3}$$

$$\rho_{yx}(B) = \frac{(n\mu_n + p\mu_p) + (n\mu_p + p\mu_n)\mu_n\mu_p B^2}{e\left[(n\mu_n + p\mu_p)^2 + (p-n)^2\mu_n^2\mu_p^2 B^2\right]}, \tag{4}$$

where the electron (hole) density and mobility are given by n (p) and μ_n (μ_p), respectively. An MoTe$_2$ sample that is 40 nm thick has similar behaviour to bulk MoTe$_2$, and so the two-band model is used. The two-band model fit is calculated from the $\rho_{xx}(B)$ and $\rho_{yx}(B)$ curves shown in Figure 27 (refer to work by Zhong *et al.* for details) [84]. The electron (hole) carrier density decreases from a value of 2.43×10^{20} cm^{-3} (2.51×10^{20} cm^{-3}) before irradiation to 1.88×10^{20} cm^{-3} (2.26×10^{20} cm^{-3}) after irradiation (Table 1). Similarly, the electron (hole) mobility decreases from 6600 cm$^2 \cdot$V$^{-1} \cdot$s^{-1} (1500 cm$^2 \cdot$V$^{-1} \cdot$s^{-1}) before irradiation to 1100 cm$^2 \cdot$V$^{-1} \cdot$s^{-1} (700 cm$^2 \cdot$V$^{-1} \cdot$s^{-1}) after irradiation. Both carrier densities decrease slightly, but not by a factor equivalent to the order of magnitude by which the transverse resistivity increases. The electron mobility does decrease significantly and, together with the decrease in carrier density, account for the increase in transverse resistivity.

Table 1: Carrier densities and mobilities from two-band model fit.

	n (cm^{-3})	p (cm^{-3})	μ_n (cm$^2 \cdot$V$\cdot^{-1} \cdot$s^{-1})	μ_p (cm$^2 \cdot$V$^{-1} \cdot$s^{-1})
Before Irradiation	2.43×10^{20}	2.51×10^{20}	6600	1500
After Irradiation	1.88×10^{20}	2.26×10^{20}	1100	700
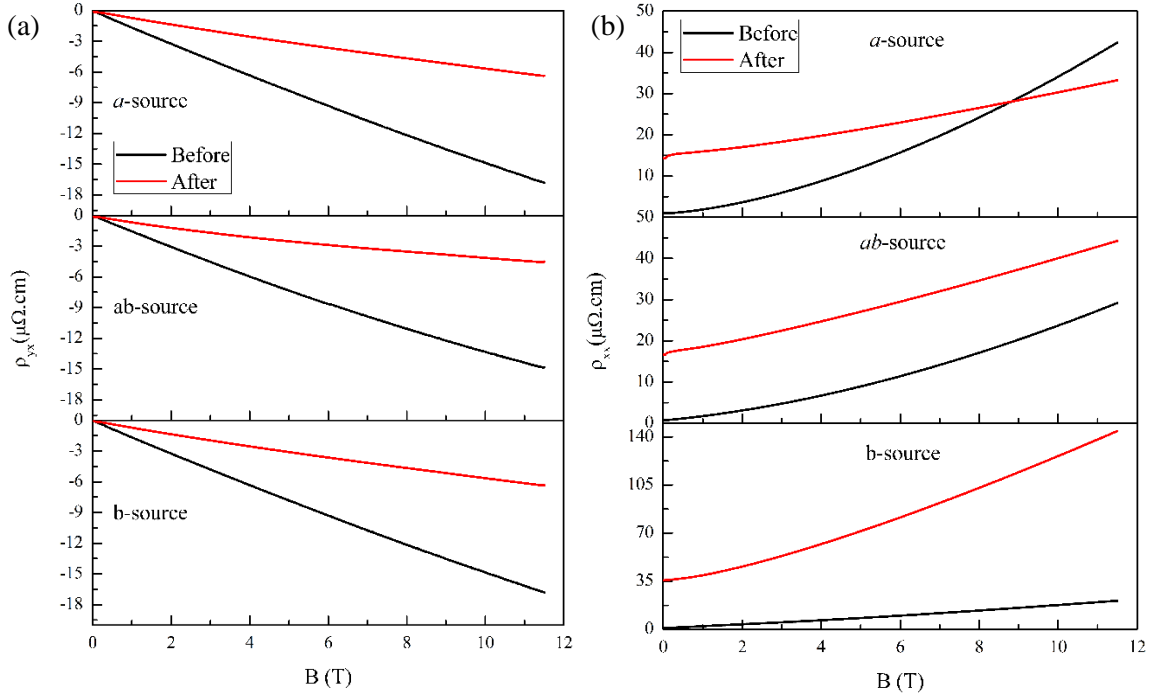
Figure 27: 40 nm MoTe₂ sample. a) Transverse resistivity (ρ_{yx}) and Longitudinal resistivity (ρ_{xx}) before and after irradiation for each source direction.

The MR is calculated using $MR(\%) = \frac{\rho(B)-\rho(0)}{\rho(0)} x 100\%$ and plotted for each orientation in Figure 28 [84]. In an externally applied magnetic field, the highest MR value between the three orientations is expected to align with the *a*-axis in the MoTe₂ crystalline structure, hence the naming convention [83]. Giant MR has been observed in bulk MoTe₂ at low temperature and is attributed to the compensation of electron and hole carrier densities [87], [90]. The calculated MR values show that the sample becomes more resistive after irradiation. This can be explained by an imbalance in the electron and hole carrier densities or by a decrease in the carrier mobilities. The carrier densities and mobilities calculated from the two-band fit suggests that the decrease in mobility is the cause.
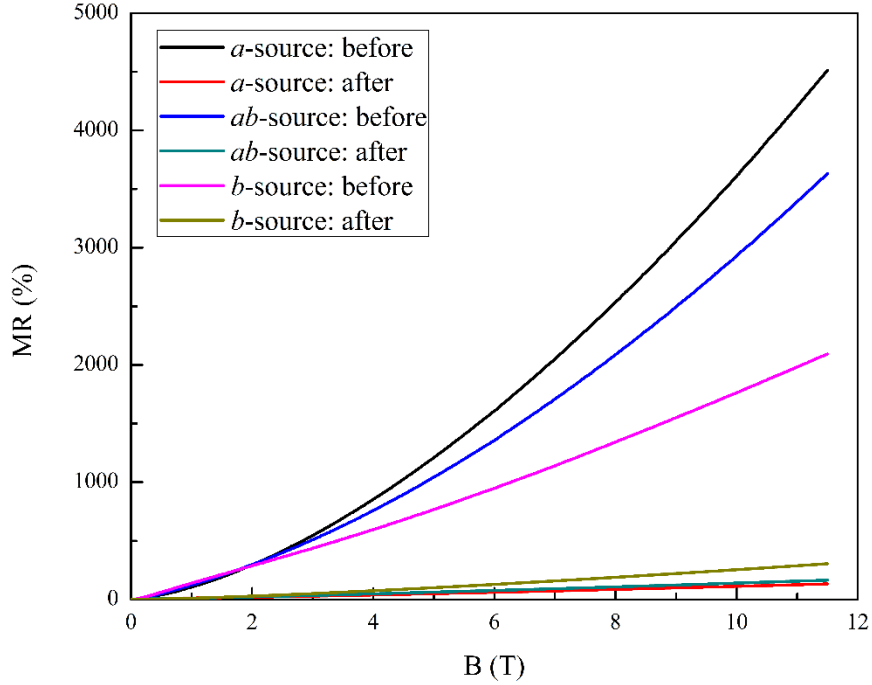
Figure 28: MR (%) before and after irradiation.

4.5 Discussion

The bb-fs-TA measurements indicate a structural change in T_d-MoTe$_2$ at high fluences where the frequency mode at ~13 cm^{-1} is absent (characteristic of 1T'-MoTe$_2$), with damping times averaging ~4.5 ps (characteristic of T_d-MoTe$_2$). The mode at ~13 cm^{-1} corresponds to an interlayer shear mode whereas the other observable modes at ~77 cm^{-1} and ~164 cm^{-1} correspond to intralayer vibrational modes. This suggests that the light-induced structural change primarily affected the interlayer orientation of the layers since the ~13 cm^{-1} mode is destroyed. This is corroborated by the magnetotransport measurements. The sample becomes more resistive due lower mobility and/or carrier density and SdH oscillations are no longer present. These features point to a more disordered state, which may also be the origin of its durability. Thus, there remains the question of whether this structural change is simply a disordered version of T_d-MoTe$_2$, or if it possesses unique optical and/or transport properties. Future work will include transport measurements ~200 K, which is closer to the experimental conditions of the bb-fs-TA spectroscopy measurements. Since the structural change has so far demonstrated durability, other characterization techniques should ideally be employed. For example, TEM or angle-resolved photoemission spectroscopy (ARPES) measurements could offer complementary information about this unique structure in MoTe$_2$.

Bibliography

[1] K. S. Novoselov *et al.*, "Electric Field Effect in Atomically Thin Carbon Films," *Science*, vol. 306, no. 5696, pp. 666–669, Oct. 2004.

[2] "The Nobel Prize in Physics 2010," *NobelPrize.org*. [Online]. Available: https://www.nobelprize.org/prizes/physics/2010/press-release/. [Accessed: 17-Feb-2019].

[3] S. Z. Butler *et al.*, "Progress, Challenges, and Opportunities in Two-Dimensional Materials Beyond Graphene," *ACS Nano*, vol. 7, no. 4, pp. 2898–2926, Apr. 2013.

[4] K. F. Mak and J. Shan, "Photonics and optoelectronics of 2D semiconductor transition metal dichalcogenides," *Nat. Photonics*, vol. 10, no. 4, pp. 216–226, Apr. 2016.

[5] J. S. Ross *et al.*, "Interlayer Exciton Optoelectronics in a 2D Heterostructure p–n Junction," *Nano Lett.*, vol. 17, no. 2, pp. 638–643, Feb. 2017.

[6] J. Ping, Z. Fan, M. Sindoro, Y. Ying, and H. Zhang, "Recent Advances in Sensing Applications of Two-Dimensional Transition Metal Dichalcogenide Nanosheets and Their Composites," *Adv. Funct. Mater.*, vol. 27, no. 19, p. 1605817, 2017.

[7] J. R. Schaibley *et al.*, "Valleytronics in 2D materials," *Nat. Rev. Mater.*, vol. 1, no. 11, p. 16055, Nov. 2016.

[8] K. F. Mak, K. He, J. Shan, and T. F. Heinz, "Control of valley polarization in monolayer MoS_2 by optical helicity," *Nat. Nanotechnol.*, vol. 7, no. 8, pp. 494–498, Aug. 2012.

[9] L. Bawden *et al.*, "Spin–valley locking in the normal state of a transition-metal dichalcogenide superconductor," *Nat. Commun.*, vol. 7, p. 11711, May 2016.

[10] W. Chen, R. Liang, J. Wang, and J. Xu, "Precisely controllable n-type doping in MoTe2 field effect transistors by hydrazine treatment," *Appl. Phys. Lett.*, vol. 113, no. 15, p. 152102, Oct. 2018.

[11] M. Sato and S. Fujimoto, "Topological phases of noncentrosymmetric superconductors: Edge states, Majorana fermions, and non-Abelian statistics," *Phys. Rev. B*, vol. 79, no. 9, p. 094504, Mar. 2009.

[12] Y. Sun, S.-C. Wu, M. N. Ali, C. Felser, and B. Yan, "Prediction of Weyl semimetal in orthorhombic MoTe2," *Phys. Rev. B*, vol. 92, no. 16, p. 161107, Oct. 2015.

[13] Z. Wang *et al.*, MoTe2: A Type-II Weyl Topological Metal," *Phys. Rev. Lett.*, vol. 117, no. 5, p. 056805, Jul. 2016.

[14] R. F. Frindt, "Superconductivity in Ultrathin NbSe2 Layers," *Phys. Rev. Lett.*, vol. 28, no. 5, pp. 299–301, Jan. 1972.

[15] B. Sipos, A. F. Kusmartseva, A. Akrap, H. Berger, L. Forró, and E. Tutiš, "From Mott state to superconductivity in 1T-TaS_2," *Nat. Mater.*, vol. 7, no. 12, pp. 960–965, Dec. 2008.

[16] J. M. Lu *et al.*, "Evidence for two-dimensional Ising superconductivity in gated MoS2," *Science*, vol. 350, no. 6266, pp. 1353–1357, Dec. 2015.

[17] X. Xi *et al.*, "Ising pairing in superconducting $NbSe_2$ atomic layers," *Nat. Phys.*, vol. 12, no. 2, pp. 139–143, Feb. 2016.

[18] G.-B. Liu, D. Xiao, Y. Yao, X. Xu, and W. Yao, "Electronic structures and theoretical modelling of two-dimensional group-VIB transition metal dichalcogenides," *Chem. Soc. Rev.*, vol. 44, no. 9, pp. 2643–2663, Apr. 2015.

[19] A. V. Kolobov, P. Fons, and J. Tominaga, "Electronic excitation-induced semiconductor-to-metal transition in monolayer MoTe2," *Phys. Rev. B*, vol. 94, no. 9, p. 094114, Sep. 2016.

[20] A. Splendiani *et al.*, "Emerging Photoluminescence in Monolayer MoS2," *Nano Lett.*, vol. 10, no. 4, pp. 1271–1275, Apr. 2010.

[21] I. G. Lezama *et al.*, "Indirect-to-Direct Band Gap Crossover in Few-Layer MoTe2," *Nano Lett.*, vol. 15, no. 4, pp. 2336–2342, Apr. 2015.

[22] M. Zhang and G. West, "Berry curvature and symmetry broken induced Hall effect in MoS2," *ArXiv180305325 Cond-Mat*, Mar. 2018.

[23] C. J. Ciccarino, T. Christensen, R. Sundararaman, and P. Narang, "Dynamics and Spin-Valley Locking Effects in Monolayer Transition Metal Dichalcogenides," *Nano Lett.*, vol. 18, no. 9, pp. 5709–5715, Sep. 2018.

[24] J. H. Jung, C.-H. Park, and J. Ihm, "A Rigorous Method of Calculating Exfoliation Energies from First Principles," *Nano Lett.*, Apr. 2018.

[25] A. W. Tsen *et al.*, "Structure and control of charge density waves in two-dimensional 1T-TaS2," *Proc. Natl. Acad. Sci.*, vol. 112, no. 49, pp. 15054–15059, Dec. 2015.

[26] N. Alem, R. Erni, C. Kisielowski, M. D. Rossell, W. Gannett, and A. Zettl, "Atomically thin hexagonal boron nitride probed by ultrahigh-resolution transmission electron microscopy," *Phys. Rev. B*, vol. 80, no. 15, p. 155425, Oct. 2009.

[27] D. Pacilé, J. C. Meyer, Ç. Ö. Girit, and A. Zettl, "The two-dimensional phase of boron nitride: Few-atomic-layer sheets and suspended membranes," *Appl. Phys. Lett.*, vol. 92, no. 13, p. 133107, Mar. 2008.

[28] M. Yankowitz, Q. Ma, P. Jarillo-Herrero, and B. J. LeRoy, "van der Waals heterostructures combining graphene and hexagonal boron nitride," *Nat. Rev. Phys.*, vol. 1, no. 2, p. 112, Feb. 2019.

[29] J. Bao *et al.*, "Synthesis and applications of two-dimensional hexagonal boron nitride in electronics manufacturing," *Electron. Mater. Lett.*, vol. 12, no. 1, pp. 1–16, Jan. 2016.

[30] A. Ciarrocchi, D. Unuchek, A. Avsar, K. Watanabe, T. Taniguchi, and A. Kis, "Control of interlayer excitons in two-dimensional van der Waals heterostructures," *ArXiv180306405 Cond-Mat*, Mar. 2018.

[31] T. Deilmann and K. S. Thygesen, "Interlayer Excitons with Large Optical Amplitudes in Layered van der Waals Materials," *Nano Lett.*, Apr. 2018.

[32] M. M. Ugeda *et al.*, "Characterization of collective ground states in single-layer NbSe2," *Nat. Phys.*, vol. 12, no. 1, pp. 92–97, Jan. 2016.

[33] B. T. Zhou, N. F. Q. Yuan, H.-L. Jiang, and K. T. Law, "Ising superconductivity and Majorana fermions in transition-metal dichalcogenides," *Phys. Rev. B*, vol. 93, no. 18, p. 180501, May 2016.

[34] S. C. de la Barrera *et al.*, "Tuning Ising superconductivity with layer and spin–orbit coupling in two-dimensional transition-metal dichalcogenides," *Nat. Commun.*, vol. 9, no. 1, p. 1427, Apr. 2018.

[35] E. Sohn *et al.*, "An unusual continuous paramagnetic-limited superconducting phase transition in 2D NbSe 2," *Nat. Mater.*, vol. 17, no. 6, pp. 504–508, Jun. 2018.

[36] B. Huang *et al.*, "Layer-dependent Ferromagnetism in a van der Waals Crystal down to the Monolayer Limit," *Nature*, vol. 546, no. 7657, pp. 270–273, Jun. 2017.

[37] W.-B. Zhang, Q. Qu, P. Zhu, and C.-H. Lam, "Robust Intrinsic Ferromagnetism and Half Semiconductivity in Stable Two-Dimensional Single-Layer Chromium Trihalides," *J Mater Chem C*, vol. 3, no. 48, pp. 12457–12468, 2015.

[38] A. A. Soluyanov *et al.*, "Type-II Weyl semimetals," *Nature*, vol. 527, no. 7579, pp. 495–498, Nov. 2015.

[39] K. Zhang *et al.*, "Raman signatures of inversion symmetry breaking and structural phase transition in type-II Weyl semimetal MoTe2," *Nat. Commun.*, vol. 7, p. 13552, Dec. 2016.

[40] A. Castellanos-Gomez *et al.*, "Deterministic transfer of two-dimensional materials by all-dry viscoelastic stamping," *2D Mater.*, vol. 1, no. 1, p. 011002, 2014.

[41] T. Uwanno, Y. Hattori, T. Taniguchi, K. Watanabe, and K. Nagashio, "Fully dry PMMA transfer of graphene on h-BN using a heating/cooling system," *ArXiv151107117 Cond-Mat*, Nov. 2015.

[42] S. J. Kim *et al.*, "Ultraclean Patterned Transfer of Single-Layer Graphene by Recyclable Pressure Sensitive Adhesive Films," *Nano Lett.*, vol. 15, no. 5, pp. 3236–3240, May 2015.

[43] X. Ma *et al.*, "Capillary-Force-Assisted Clean-Stamp Transfer of Two-Dimensional Materials," *Nano Lett.*, Oct. 2017.

[44] P. J. Zomer, M. H. D. Guimarães, J. C. Brant, N. Tombros, and B. J. van Wees, "Fast pick up technique for high quality heterostructures of bilayer graphene and hexagonal boron nitride," *Appl. Phys. Lett.*, vol. 105, no. 1, p. 013101, Jul. 2014.

[45] F. Pizzocchero *et al.*, "The hot pick-up technique for batch assembly of van der Waals heterostructures," *Nat. Commun.*, vol. 7, p. ncomms11894, Jun. 2016.

[46] L. Wang *et al.*, "One-Dimensional Electrical Contact to a Two-Dimensional Material," *Science*, vol. 342, no. 6158, pp. 614–617, Nov. 2013.

[47] R. T. Tung, "Chemical Bonding and Fermi Level Pinning at Metal-Semiconductor Interfaces," *Phys. Rev. Lett.*, vol. 84, no. 26, pp. 6078–6081, Jun. 2000.

[48] H. Liu *et al.*, "Switching Mechanism in Single-Layer Molybdenum Disulfide Transistors: An Insight into Current Flow across Schottky Barriers," *ACS Nano*, vol. 8, no. 1, pp. 1031–1038, Jan. 2014.

[49] L. Yang *et al.*, "Chloride Molecular Doping Technique on 2D Materials: WS2 and MoS2," *Nano Lett.*, vol. 14, no. 11, pp. 6275–6280, Nov. 2014.

[50] R. Kappera *et al.*, "Phase-engineered low-resistance contacts for ultrathin MoS_2 transistors," *Nat. Mater.*, vol. 13, no. 12, p. 1128, Dec. 2014.

[51] P. Blake *et al.*, "Making graphene visible," *Appl. Phys. Lett.*, vol. 91, no. 6, p. 063124, Aug. 2007.

[52] H. H. Kim *et al.*, "Evolution of interlayer and intralayer magnetism in three atomically thin chromium trihalides," *ArXiv190301409 Cond-Mat*, Mar. 2019.

[53] M. Tinkham, *Introduction to Superconductivity*. Courier Corporation, 2004.

[54] J. Bardeen, L. N. Cooper, and J. R. Schrieffer, "Theory of Superconductivity," *Phys. Rev.*, vol. 108, no. 5, pp. 1175–1204, Dec. 1957.

[55] A. M. Clogston, "Upper Limit for the Critical Field in Hard Superconductors," *Phys. Rev. Lett.*, vol. 9, no. 6, pp. 266–267, Sep. 1962.

[56] B. S. Chandrasekhar, "A note on the maximum critical field of high-field superconductors," *Appl. Phys. Lett.*, vol. 1, no. 1, pp. 7–8, Sep. 1962.

[57] E. Khestanova *et al.*, "Unusual suppression of the superconducting energy gap and critical temperature in atomically thin NbSe2," *ArXiv180304920 Cond-Mat*, Mar. 2018.

[58] X. Xi *et al.*, "Strongly enhanced charge-density-wave order in monolayer NbSe2," *Nat. Nanotechnol.*, vol. 10, no. 9, pp. 765–769, Sep. 2015.

[59] D. Möckli and M. Khodas, "Robust parity-mixed superconductivity in disordered monolayer transition metal dichalcogenides," *Phys. Rev. B*, vol. 98, no. 14, p. 144518, Oct. 2018.

[60] S. Chikazumi, *Physics of Ferromagnetism 2e*. OUP Oxford, 2009.

[61] R. B. Griffiths, "Peierls Proof of Spontaneous Magnetization in a Two-Dimensional Ising Ferromagnet," *Phys. Rev.*, vol. 136, no. 2A, pp. A437–A439, Oct. 1964.

[62] C. A. F. Vaz, J. A. C. Bland, and G. Lauhoff, "Magnetism in ultrathin film structures," *Rep. Prog. Phys.*, vol. 71, no. 5, p. 056501, Apr. 2008.

[63] N. D. Mermin and H. Wagner, "Absence of Ferromagnetism or Antiferromagnetism in One- or Two-Dimensional Isotropic Heisenberg Models," *Phys. Rev. Lett.*, vol. 17, no. 22, pp. 1133–1136, Nov. 1966.

[64] T. Thomson, "10 - Magnetic properties of metallic thin films," in *Metallic Films for Electronic, Optical and Magnetic Applications*, K. Barmak and K. Coffey, Eds. Woodhead Publishing, 2014, pp. 454–546.

[65] M.-W. Lin *et al.*, "Ultrathin nanosheets of CrSiTe3: a semiconducting two-dimensional ferromagnetic material," *J. Mater. Chem. C*, vol. 4, no. 2, pp. 315–322, Dec. 2015.

[66] N. Sivadas, M. W. Daniels, R. H. Swendsen, S. Okamoto, and D. Xiao, "Magnetic ground state of semiconducting transition-metal trichalcogenide monolayers," *Phys. Rev. B*, vol. 91, no. 23, p. 235425, Jun. 2015.

[67] B. Sachs, T. O. Wehling, K. S. Novoselov, A. I. Lichtenstein, and M. I. Katsnelson, "Ferromagnetic two-dimensional crystals: Single layers of K2CuF4," *Phys. Rev. B*, vol. 88, no. 20, p. 201402, Nov. 2013.

[68] L. Webster and J.-A. Yan, "Strain-tunable magnetic anisotropy in monolayer CrCl3, CrBr3, and CrI3," *Phys. Rev. B*, vol. 98, no. 14, p. 144411, Oct. 2018.

[69] C. Huang, Y. Du, H. Wu, H. Xiang, K. Deng, and E. Kan, "Prediction of Intrinsic Ferromagnetic Ferroelectricity in a Transition-Metal Halide Monolayer," *Phys. Rev. Lett.*, vol. 120, no. 14, p. 147601, Apr. 2018.

[70] J. S. Moodera, G.-X. Miao, and T. S. Santos, "Frontiers in spin-polarized tunneling," *Phys. Today*, vol. 63, no. 4, pp. 46–51, Apr. 2010.

[71] P. M. Tedrow and R. Meservey, "Spin-Dependent Tunneling into Ferromagnetic Nickel," *Phys. Rev. Lett.*, vol. 26, no. 4, pp. 192–195, Jan. 1971.

[72] G.-X. Miao, M. Münzenberg, and J. S. Moodera, "Tunneling path toward spintronics," *Rep. Prog. Phys.*, vol. 74, no. 3, p. 036501, Feb. 2011.

[73] G.-X. Miao, M. Müller, and J. S. Moodera, "Magnetoresistance in Double Spin Filter Tunnel Junctions with Nonmagnetic Electrodes and its Unconventional Bias Dependence," *Phys. Rev. Lett.*, vol. 102, no. 7, p. 076601, Feb. 2009.

[74] J. S. Moodera, T. S. Santos, and T. Nagahama, "The phenomena of spin-filter tunnelling," *J. Phys. Condens. Matter*, vol. 19, no. 16, p. 165202, 2007.

[75] H. H. Kim *et al.*, "One Million Percent Tunnel Magnetoresistance in a Magnetic van der Waals Heterostructure," *Nano Lett.*, Jul. 2018.

[76] T. Song *et al.*, "Giant tunneling magnetoresistance in spin-filter van der Waals heterostructures," *Science*, vol. 360, no. 6394, pp. 1214–1218, Jun. 2018.

[77] S. Lounis, "Theory of Scanning Tunneling Microscopy," *ArXiv14040961 Cond-Mat*, Apr. 2014.

[78] H. Wang *et al.*, "High-quality monolayer superconductor NbSe2 grown by chemical vapour deposition," *Nat. Commun.*, vol. 8, no. 1, p. 394, Aug. 2017.

[79] C.-Z. Xu *et al.*, "Experimental and theoretical electronic structure and symmetry effects in ultrathin NbSe2 films," *Phys. Rev. Mater.*, vol. 2, no. 6, p. 064002, Jun. 2018.

[80] A. Crepaldi *et al.*, "Enhanced ultrafast relaxation rate in the Weyl semimetal phase of MoTe2 measured by time-and angle-resolved photoelectron spectroscopy," *ArXiv170909854 Cond-Mat*, Sep. 2017.

[81] R. He *et al.*, "Dimensionality-driven orthorhombic MoTe2 at room temperature," *ArXiv180101217 Cond-Mat*, Jan. 2018.

[82] S. Mallat, *A Wavelet Tour of Signal Processing: The Sparse Way*. Academic Press, 2008.

[83] Y.-Y. Lv *et al.*, "The relationship between anisotropic magnetoresistance and topology of Fermi surface in Td-MoTe2 crystal," *J. Appl. Phys.*, vol. 122, no. 4, p. 045102, Jul. 2017.

[84] S. Zhong *et al.*, "Origin of magnetoresistance suppression in thin gamma-MoTe2," *Phys. Rev. B*, vol. 97, no. 24, p. 241409, Jun. 2018.

[85] D. E. Soule, J. W. McClure, and L. B. Smith, "Study of the Shubnikov-de Haas Effect. Determination of the Fermi Surfaces in Graphite," *Phys. Rev.*, vol. 134, no. 2A, pp. A453–A470, Apr. 1964.

[86] X. Luo *et al.*, "Td-MoTe2: A possible topological superconductor," *Appl. Phys. Lett.*, vol. 109, no. 10, p. 102601, Sep. 2016.

[87] Q. Zhou, D. Rhodes, Q. R. Zhang, S. Tang, R. Schönemann, and L. Balicas, "Hall effect within the colossal magnetoresistive semimetallic state of MoTe2," *Phys. Rev. B*, vol. 94, no. 12, p. 121101, Sep. 2016.

[88] J. M. Ziman, *Electrons and Phonons: The Theory of Transport Phenomena in Solids*. OUP Oxford, 2001.

[89] N. W. Ashcroft and N. D. Mermin, *Solid State Physics*. Holt, Rinehart and Winston, 1976.

[90] F. C. Chen *et al.*, "Extremely large magnetoresistance in the type-II Weyl semimetal MoTe2," *Phys. Rev. B*, vol. 94, no. 23, p. 235154, Dec. 2016.

Appendix A

Thickness of NbSe$_2$ in SFTJ Device

Figure S1a shows an optical image of the NbSe$_2$ flake used in the SFTJ device fabrication. Based on the optical contrast, the flake is estimated to be ~8-10 nm thick. Figure S1b shows an optical image of the device after removing the PC layer. Some damage to the hBN, or an embedded piece of debris is very close to the overlap area of the device. This impedes an accurate measurement of the NbSe$_2$ flake thickness by AFM. The AFM image is shown in Figure S1c with an outline of the location of the NbSe$_2$ flake drawn in. The thickness of the flake can only be measured from top to bottom or *vice versa*. A lateral profile across the flake would not be the true thickness since the NbSe$_2$ is below Gr and CrBr$_3$, but above the Gr flake on the left.
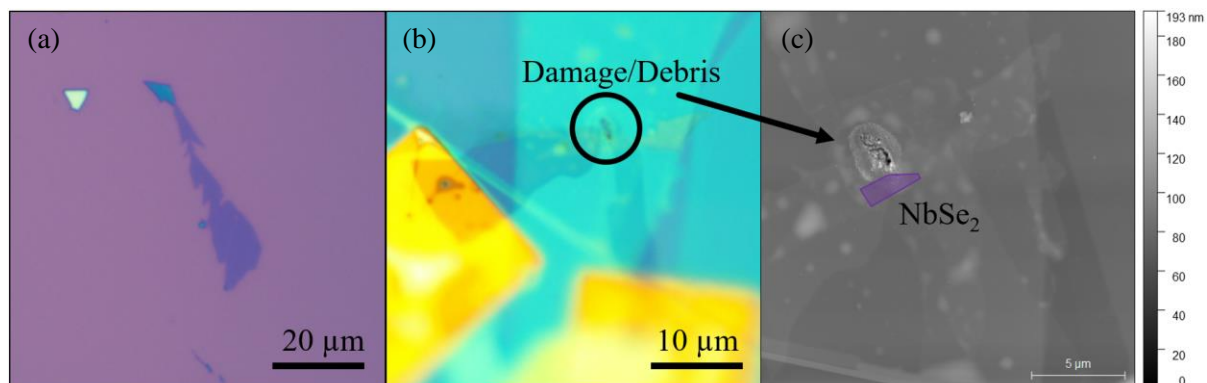

Figure S1: a) optical image of NbSe$_2$ flake used for SFTJ device; b) optical image of device after removing PC; c) AFM image of device. Damage/debris on the hBN near the NbSe$_2$ introduces error to the measurement.

Appendix B

Conductance Curves at Different $B_\perp$ and $B_\parallel$

Figure S2 shows the conductance curves for the sample at 0.5 T at different angles (blue curves). These curves are plotted for each component (angle) against the conductance for the sample in a completely out-of-plane field ($B_{//} = 0$) with the same magnitude of each component (black curves). The conductance curves that contain an in-plane field component are slightly enhanced.
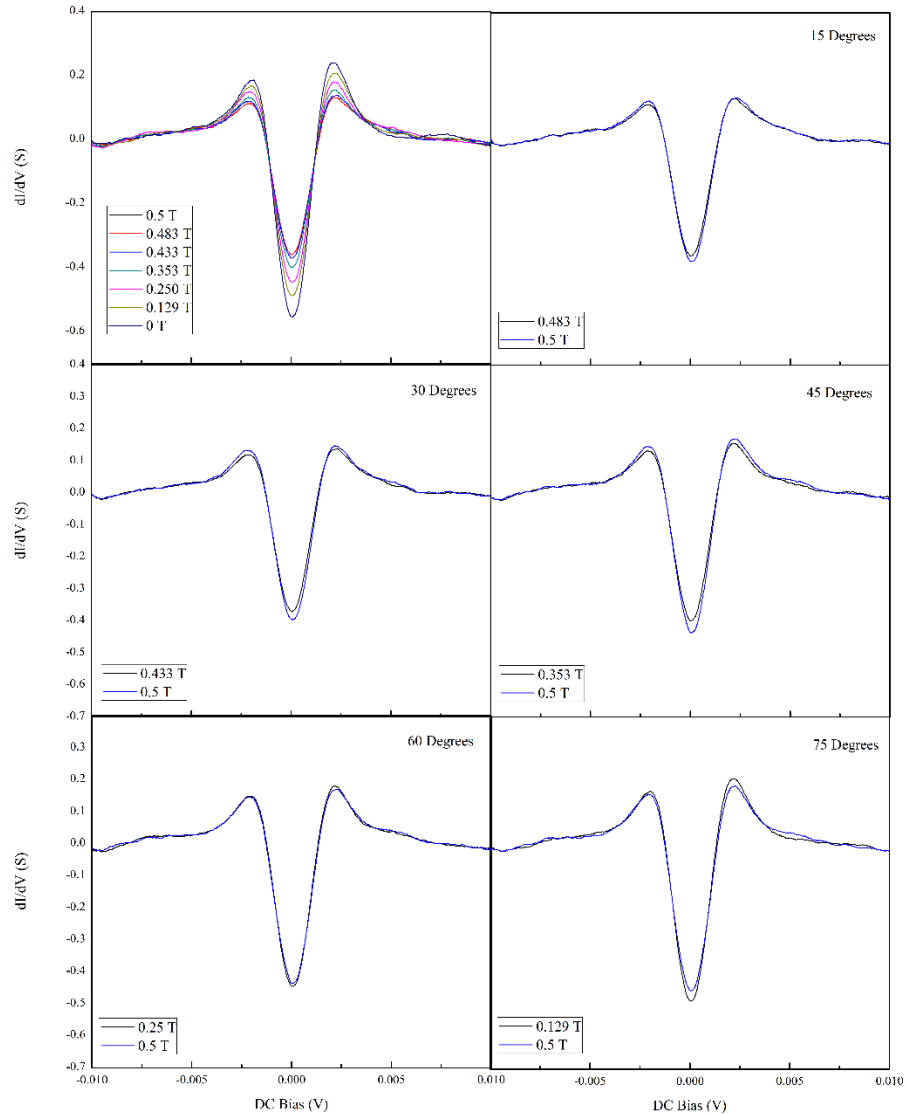
Figure S2: Angle measurements and out-of-plane magnetic field components for 0.5 T.